A neural network approach for elucidating fluid leakage along hard-linked normal faults

Priyadarshi Chinmoy Kumar[1, 2, a], Kamal'deen O. Omosanya[3,4 b], Tiago M. Alves[5, c] and Kalachand Sain[1,2, 6, d]

[1]CSIR-National Geophysical Research Institute, Hyderabad, India
[2]Academy of Scientific and Innovative Research-NGRI, Hyderabad, India
[3]Timelapsegeo, Stiklestadveien 1, 7041 Trondheim
[4]Oasis Geoconsulting Limited, Ogun State, Nigeria
[5]3D Seismic Lab, Cardiff University, Cardiff, UK
[5]Wadia Institute of Himalayan Geology, Dehradun, India
[a]kumarchinmoy@gmail.com; [b]kamaloomosanya@yahoo.com; [c]alvest@cardiff.ac.uk; [d]kalachandsain@yahoo.com

Corresponding author: kumarchinmoy@gmail.com

Abstract

Increasing displacement and strain accumulation in normal faults can result in the formation of hard-linked structures that are preferred loci for fluid leakage. Three-dimensional seismic data from offshore New Zealand reveals Miocene geological units that were structurally deformed to form several hard-linked fault zones. Fluids are observed to migrate through these breached zones into younger strata. Here, we use an automated approach by designing two different meta-attributes, the Thinned Fault (TFC) and Fluid (FC) Cubes, to capture the detailed geometry of hard-linked fault zones, and of fluid flowing through these same structures. The two meta-attributes are prepared through an amalgamation of different seismic attributes, which are trained based on the interpreter's skills and experience following a supervised scheme of neural learning. The meta-attributes enhance sub-surface geological features and reveal their structural geometries. Faults in the study area are therefore observed to strike to the NE with different geometries, e.g. forming curved shapes (F1 and F2), sigmoid shapes (F3), and Y shapes (F4). Relay ramps between these faults are intensively breached, allowing for important fluid migration through hard-linked structures. We demonstrate that our interpretation approach does not only honour the interpreter's knowledge about key geological processes, but also adds value in revealing the 3D architecture of hard-linked normal faults.

Keywords: New Zealand; Taranaki Basin; Hard-linked faults; seismic attributes; Neural Networks

1. Introduction

Hard-linked faults comprise structures in which a breaching fault cuts and displaces a relay ramp formed between two adjacent, larger faults (Larsen, 1988; Peacock and Sanderson, 1994). In contrast, soft-linked faults are structures in which a relay ramp is formed and remains relatively undeformed. The primary factors that control the breaching of a relay ramp are the slip vectors of overlapping faults, their spacing and relative displacement (Pollard and Aydin, 1984; Peacock and Sanderson, 1994; Peacock et al., 2000; Ferrill and Morris, 2001). In extensional regimes, relay ramps are formed initially in low strain conditions. At a later stage, when the strain progressively accumulates, the relay ramp starts to deform internally and is breached by several faults and smaller structures (Larsen, 1988; Peacock, 1991, 1994; Kristensen et al., 2013; Fossen and Rotevatn, 2016). Importantly, the degree of deformation that is experienced in relay ramps greatly depends on the mechanical rock properties of faulted rocks at the time of deformation (Aydin et al., 2006; Fossen et al., 2007)

Relay ramps in hard-linked fault zones are structurally complex, comprising multiple faults and fractures (Sibson, 1996; Peacock and Parfitt, 2002; Kim et al., 2004; Fossen et al., 2005). These faults and fractures can act as pathways for the vertical migration of fluids such as hydrocarbons, CO_2, hydrothermal solutions, metamorphic fluids, magmatic fluids and ground water (Breit and Meunier, 1990; Curewitz and Karson, 1997; Rowland and Sibson, 2004; Dini et al., 2008; Sharp et al., 2010; Dockrill and Shipton, 2010). In hydrocarbon exploration, relay ramps are not only important to the accumulation and trapping of hydrocarbons, but also have a negative impact on seal integrity (Gartrell et al., 2004; Kristiansen, 2011). Fault-controlled (structural) hydrocarbon traps are generally underfilled or dry wherever the seal is controlled by two or more interacting faults (Kristiansen, 2011). In parallel, fault intersections, or intensive breaching within fault-controlled structural traps, usually comprise leakage zones for hydrocarbons (Gartrell, 2004).

The use of high quality 3-D seismic reflection data has opened new avenues to better understand the history of hard-linked fault zones, especially when fluid leakage is associated with such structures (Coward et al., 1998; Bense and Baalen, 2004; Manzoochi et al., 2008; Rotevatn et al., 2007; Alarfaj and Lawton, 2012; Mohammedyasin, 2015). Several authors have documented different interpretation techniques that enhance the interpretation of such hard-linked fault zones (e.g., Pedersen et a., 2002, 2003; Cohen et al., 2006; Wu and Zhu,

2017; Huang et al., 2017; Lu et al., 2018; Wu et al., 2019b). Seismic attributes can thus be applied to characterise the response of seismic waves in these geological structures, identifying fluid migration pathways (Alarfaj and Lawton, 2012; Mohammedyasin, 2015), but these attributes are chiefly used in the literature to assist 'conventional' interpretation workflows that rely on manual interpretation. Since faults are normally associated with breaks in seismic reflection, and often appear as linear, sub-linear or curvilinear features (Shaw et al., 2005; Iacopini and Butler, 2011; Jaglan et al. 2015), to accurately position and interpret them becomes a tedious task (Kumar and Mandal, 2017; Kumar and Sain, 2018). Moreover, the quality of seismic attributes used in the mapping of discontinuities, such as seismic semblance or coherency, essentially relies on the different parameters (step-outs, time windows, input data etc.) used in their computation (Kumar et al., 2019a). To complement these conventional interpretation approaches, Mohammedyasin et al. (2015) used an advanced interpretation method involving the computation of a volume probe to show escaping fluid from seismic data in the Snøhvit Gas Field, Hammerfest Basin. A common downside of this latter technique is the inability of an attribute (e.g. seismic amplitude) to respond to a certain geological phenomenon within the seismic volume. This caveat often results in the overlapping of several geological bodies along desired targets, thus hindering consistent structural interpretations.

The present study introduces an automated approach for elucidating fluid leakage through discontinuous geological structures. In detail we developed two meta-attributes, called the Thinned Fault (TFC) and Fluid (FC) Cubes, using a high-resolution, high-quality, 3-D seismic volume from New Zealand (Fig. 1). To achieve the aims of this study, a well-known natural site was chosen whereby the presence of hard-linked faults is well documented, i.e. the Parihaka prospect, offshore Taranaki Basin (Figs. 1 and 2). The stratigraphic interval of interest comprises the Oligocene Tikorangi Formation and the Miocene Monganui and Moki Formations (Fig. 3). The workflow and methods adopted in this work are automated and not laborious, leading to an enhanced interpretation of hard-linked faults and vertical fluid migration. The strength of our approach is in the integration of the artificial intelligence of Neural Networks with the interpreters' skills and experience, ultimately streamlining any interpretation workflow.

2. Tectonic evolution and geology of the study area

The study area is the Taranaki Basin, which is ~60 km wide and extends ~350 km in a NNE direction, from south of the Taranaki Peninsula to the offshore area west of Auckland (Fig. 1). From Late Cretaceous to Early Eocene, the Taranaki Basin recorded extensional tectonics due to the breakup of Gondwanaland and the formation of the Tasman Sea. This was followed by compression during the Late Eocene, and back-arc extension from Late Miocene to Recent

(Giba, 2012). The western part of the basin has been largely stable since the Late Eocene (Pilaar and Wakefield, 1978; Knox, 1982), while its eastern part is bounded by the Taranaki Fault (Fig. 1). In parallel, the southern part of the basin is characterised by reverse faulting and important tectonic inversion. The study area, located in the northern half of the Taranaki Basin, has undergone continuous subsidence as revealed by the numerous normal and extensional faults observed in seismic data. The northern part of the basin also comprises several intrusive magmatic bodies (Pilaar and Wakefield, 1978; Knox, 1982; King and Thrasher, 1996).

In the Late Cretaceous, several fault-bounded graben and half-graben structures (King and Thrasher, 1996; Higgs et al. 2012) related to extensional movements were filled by syn-rift strata consisting of interbedded coal measures and sandstones of the Pakawau Group (Palmer and Andrews 1993; King and Thrasher 1996) (Fig. 3). The overlying Paleocene and Eocene deposits contain late-rift and post-rift transgressive sequences, the Farewell, Kaimiro, Mangahewa and McKee Formations (King and Thrasher 1996; Higgs et al. 2012). They contain terrestrial to marginal marine strata part of the Kapuni Group (Higgs et al. 2012). Tectonic quiescence and a relative reduction in clastic sediment supply during the Oligocene led to the widespread deposition of limestones and calcareous mudstones in the Ngatoro Group, and the Otaraoa and Tikorangi Formations (King et al., 1999; King 2000). A transgressive phase followed this quiescent period and reached its climax in the Early Miocene, when the Taimana and Manganui Formations were deposited. A subsequent regressive phase started from the Middle Miocene (Wai-iti Group) through the Pliocene Rotokare Group (Giant Foresets Formation), until the present day (Higgs et al. 2012; Singh et al. 2016).

Petroleum systems in the study area

The younger Urenui Formation (~539 m thick) comprises claystones interbedded with sandstone reservoirs (Fig. 3). This unit was deposited in lower to mid bathyal environments from Late Miocene to Early Pliocene. The Moki Formation is a ~222 m thick reservoir consisting of interbedded sandstone, claystone tuff deposited during the Late Miocene (Arco Petroleum, 1992) (Fig. 3). The Monganui Formation was deposited in lower to mid bathyal environments during the Miocene and consists of interbedded tuff and claystone (Arco Petroleum, 1992). The Oligocene Tikorangi Formation is a limestone unit (Arco Petroleum, 1992) (Fig. 3). The Pakawau Group consists of carbonaceous shale and coal measures deposited during the Late Cretaceous (Arco Petroleum, 1992). Arco Petroleum (1992) documented the occurrence of hydrocarbon migration from the Pakawau Formation into reservoirs in the Moki and the younger Urenui Formation (Fig. 3). Oil and small amounts of

gas were observed within the Moki, Monganui and Urenui strata when the well Arawa-1 was drilled (Arco Petroleum, 1992).

3. Geophysical Data

The work uses 3-D time-migrated seismic data consisting of 1132 inlines (Line no. 1665 to 2797) and 2904 xlines (Line no. 2835 to 5739) acquired over the Parihaka prospect of the Taranaki Basin (Fig. 1). The seismic data was acquired in 2005 by B/V Veritas Viking II for Pogo New Zealand and covers an area of 1028.55 km^2. Additional acquisition parameters include a bin spacing of 25.0 m × 12.5m (inl/xl), a 4 ms sampling interval, a 60-fold coverage and a recording length of 6.0 s. The acquired data has been processed following conventional workflows that include trace edits, geometry updates, signal deconvolution, anomalous amplitude attenuation (AAA), multiple elimination, velocity analysis, dip move-out corrections, migration preconditioning, anisotropic Kirchhoff time migration, and common midpoint (CMP) data stacking. A three-pass velocity analysis, accompanied by a dense velocity analysis (DVA), was applied to the seismic data. The aim behind this robust processing sequence was to image deep geological structures (particularly Cretaceous strata), improve fault resolution, and reduce multiple and fault shadow effects (Western Geco, 2012). The seismic volume is displayed following the Society of Exploration Geophysicist's (SEG) American polarity, i.e. an increase in acoustic impedance is shown in black and related to a peak (or positive amplitude), while decreases in acoustic impedance boundary are shown as red reflections and correlated with troughs, or negative amplitudes. Additional geophysical data available in the study area derive from exploration wells Arawa-1, Kanuka-1, Okoki-1, Taimana-1 and Witiora-1. For this study, we used the Arawa-1 well, which was drilled to a total depth (TD) of 3055 m until the top of the Moki Formation (Arco Petroleum, 1992).

4. Research workflow

The research workflow is divided into two segments. The first segment deals with the computation and optimization of the Thin Fault Likelihood (TFL) (Fig. 4a). The second segment deals with the computation of the Thinned Fault (TFC) and Fluid (FC) Cubes (Fig. 4b).

Phase 1: Structural Conditioning

This phase is common to both workflows shown in Figs. 4a-b. Structural conditioning of the data makes seismic events laterally continuous and provides sharper structural images. Thus, to achieve our objectives, the seismic data was conditioned in three different ways.

Steering cube: a process to extract dip-azimuth information

A dip-steering process based on the phase-based dip algorithm of Tingdahl (1999), Tingdahl and de Groot (2003) and Jaglan et al. (2015), is used to compute a steering cube. This consists of a time-derived cube that contains information about seismic reflection dips and azimuth at every sample point. Different filters (i.e., 'mild, medium and coarser filters) are applied to the cube to extract the finest structural information and create 'Detailed and Background Steering Cubes'.

Structural filtering

In this step, a structure-oriented filter (SOF) is used to structurally filter the data volume by segregating the dip-azimuth of seismic reflectors and overlying random noise (Chopra and Marfurt, 2007; Hocker and Fehmers, 2002; Kumar and Mandal, 2017). This procedure helps to remove any random noise, enhance the lateral continuity of seismic events (Höcker and Fehmers, 2002; Fehmers and Höcker, 2003), and ultimately results in sharper geological structures (Kumar and Mandal, 2017; Wu and Gao, 2019). The SOF operates on three basic properties: (a) the orientation of seismic reflectors, (b) the geometry of reflection terminations, and (c) the relative preservation of these terminations, thereby smoothing seismic reflectors. Based on these principles, the seismic volume is filtered in three different stages to obtain three different conditioned seismic volumes. These filtering stages are: (i) smoothing of the seismic reflectors by applying a Dip-Steered Median Filter (DSMF), (ii) enhancement of the faults' subsurface position and geometry via a Dip-Steered Diffusion Filter (DSDF), and (iii) a logical merging of these two steps to generate Fault Enhanced Filtered (FEF) seismic data.
. During the structural filtering, seismic reflectors are first smoothed using a Dip-Steered Median Filter (DSMF) to produce DSMF seismic data. Median statistics are applied over seismic amplitudes by this filter following the stored dip-azimuth information from the Steering Cube. Hence, the masked background random noise is suppressed and seismic reflections become smoother and continuous. Later in this process, diffused reflections around fault zones are filtered using an intermediate Dip-Steered Diffusion Filter (DSDF). In this instance, a pre-computed similarity attribute derived from the original stacked seismic and Background Steering data helps the DSDF to identify linear and dissimilar seismic traces, i.e. fault zones. In the final structural filtering stage, the DSMF and the DSDF are logically merged using a cut off value of 0.5, and the similarity attribute, in order to obtain Fault Enhanced Filter (FEF) seismic data. For the TFC meta-attribute, the FEF and Detailed Steering seismic data are the main inputs, while the DSMF and Detailed Steering seismic data were used to create the FC meta-attribute.

Phase 2: Attribute Selection and Computation

Seismic attributes sensitive to faults and fractures were chosen based on the following criteria: (a) faults and discontinuities such as relay ramps are marked by abrupt changes in reflection continuity and dip (Tingdahl, 2003; Tingdahl and de Groot, 2003; Chopra and Marfurt, 2007; Roberts, 2001; Tingdahl and de Rooij, 2005; Chopra and Marfurt, 2007) and (b) fault zones are susceptible to losses in the energy and frequency content of the seismic signal (Bahorich and Farmer, 1995). Similarly, fluid migration zones in seismic data are marked by: (a) disrupted seismic reflections, (b) loss in energy content, (c) 'washing' of the higher frequency content, and (d) a dissimilar nature in seismic events (Singh et al., 2016; Omosanya et al., 2017). Knowing this, seismic attributes such as similarity, ridge enhancement filter (REF), thinned fault likelihood (TFL), reference time and signal-to-noise (S/N) ratio are grouped under the TFC meta-attribute design. Similarity, energy, average frequency and signal to noise (S/N) ratio were grouped under the FC meta-attribute design.

The thin fault likelihood (TFL) attribute (Hale, 2013; Wu and Hale, 2016) is computed using the FEF seismic data over a wide range of fault strikes and dips (Fig. 4a). In this study, the TFL is computed with 10 to 50 scans (at every 5 incremental steps) in the strike direction within a range of 0 to 360 degrees, and 15 to 55 scans (at every 5 incremental steps) in the dip direction within a range of 35 to 85 degrees. During this process, an optimised TFL is prepared to image linear faults from the seismic data. Furthermore, the similarity attribute is extracted using long (96 ms) and mid-length (48 ms) time windows. These window lengths were selected to match the orientation and vertical extent of targeted features throughout the data volume, and also to improve the detection power of the seismic attributes (Kumar and Sain, 2018). The computation of attributes is quality-checked to test their efficacy in imaging geological structures. After being quality-checked, volumetric seismic attributes are computed to be used as inputs for the neural computation (further information on the different attributes is provided in Appendices D to H).

Phase 3: Training Locations

To discriminate the input attribute responses from target and non-target zones, training locations are prepared. First, fault picks are marked as zones associated with bed displacements and associated breaks in seismic reflectors, as they are characterised by low similarity and variable dip anomalies. The non-fault picks are designated as zones that are devoid of acoustic disturbances. These locations are identified by the interpreters based on their own skills and knowledge of the local geology, the judgement of which is further corroborated (or rebuked) by seismic attribute responses.

In our study, around 3875 example locations comprising 1975 fault picks and 1900 non-fault picks, for every 10th seismic line, were selected from the seismic data. In addition, fluid migration zones were mapped based on their low similarity, low energy and 'washing-out' of frequency content. Hence, they were categorised as 'fluid picks', and the surrounding area(s) considered as 'non-fluid picks'. Approximately 1475 training locations i.e., 775 fluid picks and 700 non-fluid picks, for every 10th seismic line, were selected from the seismic data.

Phase 4: Neural Network Design

The Neural Network chosen for computing the meta-attributes is a fully connected multi-layer perceptron (MLP) network (see Meldahl et al., 2002; Aminzadeh and de Groot, 2006). The perceptron in the Neural Network are segregated into three different layers: the input layer, the hidden layer and the output layer. Inputs are fed into the network through the input layer. The processing of the data is carried out in the hidden layer, and later the outputs are extracted in the output layer. Hence, the hidden layer controls the overall structure and computational performance of the MLP network, as the number of neurons assigned to the hidden unit significantly influences the final results (Cybenko, 1989; Hornik, 1991; Hinton et al., 2006). Too many neurons in the hidden layer increase the training time and often result in problems such as overfitting, a situation where the Neural Network fits to too many a data point and fails to generalise, subsequently hindering any predictions. Therefore, it is appropriate to use a relatively small number of neurons within the hidden layer such that the computation speed is enhanced, and a faster performance of the network is guaranteed (Hornik, 1991; Hinton et al., 2006; Aminzadeh and de Groot, 2006; Singh et al., 2016).

In a multi-layer perceptron (MLP) network, the neurons within the network are interlinked with each other through synaptic weights that control and strengthen the connection. Each layer within the Neural Network consists of several neurons, thereby making the entire neural model a complex non-linear model. At this point, the use of an activation function successfully helps the non-linear mapping between inputs and their response variables (Singh et al., 2016; Kumar and Mandal, 2017; Kumar and Sain, 2018). For this reason, the MLP network in this study uses a sigmoid function that is continuous, monotonically increasing, and differentiable (Appendix A). For both the TFC and FC meta-attribute cases, the input, hidden and output layers consist of 5, 3, and 2 interconnected nodes.

The learning rate and momentum are other parameters that regulate the changes required to be incorporated into the connection links, or the weight between the different layers. These are generally assigned to the network in a trial and error basis (Poulton, 2001). In the present study, the learning rate and momentum of the Neural Network are set to 0.01 and 0.25,

respectively. Such small values in learning rates may slow down the convergence rate of the network, but help ensuring that global minima are not missed. A constant bias (node or threshold) of 1.0 is fed into the Neural Network such that the connection between the input and the processor is maintained and controlled. Accordingly, the Neural Network is made to randomly split the data into train and test sets, in which 30% of the data is used for testing and 70% is used for training. The training of the Neural Network is performed through several iterations in order to establish a minimum normalised root-mean square (nRMS) error between the two data sets, i.e. the train sets, based on interpreter's intelligence and the test sets extracted from the data, such that a probability output is obtained.

The performance evaluation of the Neural Network training is examined through normalised RMS (nRMS) error curves and misclassification percentages (Appendices B and C). The nRMS error curve demonstrates the overall error on the train and test sets. The error scale of the nRMS ranges from 0 to 1, where 0 signifies least or no error and 1 signifies the maximum error in the computed model. During the training, both error curves of the train and test data sets should initially follow a smooth decay and later continue to change in a linear fashion. If the error curve corresponding to the test data rises further, the network encounters an overfitting issue; Neural Network training should be stopped immediately before such situation happens. The misclassification percentage is also a quality control parameter that provides an estimate of the number of wrong predictions made during the classification. We follow the general rule that 'the lower is the nRMS, the lower is the misclassification percentage' (Kumar et al., 2019a, 2019b). Once this is achieved, the neural training is stopped and the output is quality-checked over key seismic lines. After a satisfactory outcome, the training is carried out over the entire data volume and this finally generates the TFC and FC meta-attributes.

Phase 5: Validation

In this phase, the results of the automatic targeted object-oriented technique are validated using the well completion reports from Arawa-1 and data published in Arco Petroleum (1992), Giba et al. (2012), Iacopini et al. (2016) and Kumar (2016).

The computation time required to execute the process is demonstrated in Table 1. The computational process was completed in a workstation with 512GB RAM and Intel Xeon E5 series dual processors, each consisting of 14 cores. All the process was run in multi-threading (parallel processing) mode.

5. Results and interpretation

5.1 Stratigraphy and basin structure

The Parihaka prospect is structurally deformed and comprises strata deposited from Late Cretaceous to the Holocene. The major fault system known as the Parihaka Normal Fault (PNF) has divided the subsurface strata into major structural compartments, the eastern and western compartments. The western compartment is highly deformed relative to the eastern compartment, consisting of series of horst-graben structures (Fig. 5). Importantly, basement units occur at a depth of 4.0 to 5.0 s Two-Way Time (TWT), being faulted and intruded by magma. The basement is overlain by the Pakawau Formation, which comprises a major source rock interval; carbonaceous shale and coal occur at a depth of 3.5 to 4.0 s TWT (Fig. 5). The reservoir succession in the Parihaka prospect comprises the Miocene Moki Formation, which is overlain by the Monganui and Mohakatino Formations. These formations are overlain by the Pliocene-Pleistocene Urenui and Giant Foreset Formations. Well Arwa-1 encountered all these stratigraphic formations and was drilled to a depth of 3055 m, i.e., the top of the Moki Formation. For this present study, the zones of interest are the Monganui, the Moki and the underlying Oligocene Tikorangi Formations that occur at depths 2.0 to 3.0 s TWT. The Monganui and Moki Formations were deposited in a lower to mid bathyal environment in the Mid to Late Miocene (Arco Petroleum, 1992). The Late Miocene is associated with back-arc extension (Giba et al., 2012). This tectonic event structurally deformed the Pariahaka prospect, giving rise to several structural compartments in the study area (Giba et al., 2012; Kumar, 2016).

5.2 Initial identification of hard-linked fault zones

The Miocene Monganui and Moki formations are faulted by NE-SW structures. At this level, the western compartment (WC) is structurally more deformed than the eastern compartment (EC). Such a deformation within the western compartment generated relay ramps between normal faults, as revealed by the similarity attribute, which demonstrates the growth and deformation of relay ramps within these geological units (Fig. 6). Relay ramps between faults F2 and F3, at a depth of 1120 ms, are devoid of any deformation (Fig. 6a). In a deeper level, 1320 ms and 1820 ms, the relay ramp experiences tectonic breaching; the ramp is breached by minute faults and discontinuous structures (Fig. 6b-c). At a depth of 2020 ms, the relay ramp between faults F2 and F3 records intensive breaching, leading to the development of a hard-linked zone (Fig. 6d).

Similar observations are made for faults F4 and F3 (Fig. 6e-h). The relay ramp between the two faults remains stable a depth of 1120 ms to 1320 ms (Fig. 6e-f). Breaching of the relay ramp begins at a depth of 1820 ms (Fig. 6g). In addition, F3 appears to be segmented and F4

develops several splays, thereby generating Y-shaped structures within this zone. At a depth of 2020 ms the relay-ramp between faults F4 and F3 records intensive breaching, leading to the development of hard-linked zones (Fig. 6h). Such an observation suggests that low tectonic strain prevailed at shallower Early Pliocene levels. Towards Mid to Late Miocene strata, high strain and increasing displacement resulted in the deformation of relay ramps, with consequent formation of several interconnected breached faults between F2 and F3, and F3 and F4. This gave rise to several hard-linked fault zones at Miocene level.

5.3 Thinned Fault Cube (TFC) and Fluid Cube (FC)

The 3-D time migrated seismic volume reveals that geological structures are prone to noisy distorted reflections, leading to poor imaging (Fig. 7a). Conditioning the data using the Dip Steered Median Filter (DSMF) smoothes the reflectors by minimising noise, and enhances the continuity of seismic events (Fig. 7b). This has improved the visibility of fault zones and several other structures in the study area. Furthermore, the application of a fault enhanced filter (FEF) added value to these observations by sharpening the interpreted structures and refining the signal strength near the fault zones. Fault edges are now sharpened, distinct and clear (Fig. 7c).

Seismic attribute analysis is used in this study to recognise structural complexity from the data volume (Figs. 8 and 9). The Thinned Fault Likelihood attribute improves the imaging of subsurface features when scanned for maximum likelihood, with several steps in the strike and dip directions (Fig. 8b-f). When scanning is increased in the strike direction from step 11 to 21, and in the dip direction from step 14 to 26, the attribute fails to capture the maximum structural detail from the seismic volume. Towards the SW, faults and minute structural features are poorly imaged in the deeper part of the section. Moreover, faults exhibit poor structural continuity and connectivity (Figs. 8b and c). Upon gradually increasing the number of scans from step 21 to 31 (strike direction) and step 26 to 34 (dip direction), a steady improvement in structural detail is observed (Fig. 5d). The TFL attribute computed for strike-dip scans 41, 50 (Fig. 8e) reveals the presence of faults in the SW and NE parts of the study area, which were previously hard to visualise (Figs. 8b to c). The faults now appear to be continuous in Fig. 8e. Further increasing the scans from step 41 to 51 in the strike direction, and step 50 to 60 in the dip direction, improves the imaging of faults and other minute structural details (Fig. 8f).

Structural features in the deeper parts of faults are efficiently captured by the TFL attribute (Fig. 8f). These observations are ascertained for an optimised case of the TFL attribute (i.e. TFL with number of strike and dip scans; 51, 60) that captures the maximum number of

structural discontinuities from the seismic volume. Attributes such as similarity and ridge enhancement filter can capture the discontinuous reflection character of the fault zones (Figs. 9a and b). The TFL attribute brings out linear fault images from the data volume (Fig. 9c).

The interval of interest in the present study (Miocene) occurs at a depth of 2.0 to 2.5 s TWT (Figs. 5). The initial interpretation of hard-linked fault zones suggested that intensive breaching of the ramps occurs at Miocene level (Figs. 7). Moreover, Arco Petroleum (1992) documented possible hydrocarbon migration from the Pakawau Formation into Moki and Urenui sandstone reservoir units. Based on these data, it can be inferred that the hard-linked fault zones acted as pathways for the migration of hydrocarbon fluid from deeper to younger strata. Attribute analysis optimally adds value to this interpretation by improving the imaging of the fluid migration pathways, as most of these pathways correspond to breached relay ramps. Thus, as similarity attribute illuminates contrasting reflection events within these pathways, distinguishing them from surrounding strata (Fig. 9d), the energy attribute suggests these zones are associated with low-amplitude and low-energy events (Fig. 9e). The higher component of frequency is washed out within the fluid migration pathways, as highlighted by the frequency attribute (Fig. 9f).

5.4 Neural Optimization of the Thinned Fault Cube (TFC) and Fluid Cube (FC)

Neural training between the test and train data sets resulted in small RMS errors and minor misclassification percentages (Figs. 10a-f). In the case of the TFC meta-attribute, after 40 iterations, the normalised RMS error and misclassification percentage for both the train and test data sets reached minimum values between 0.3-0.42 and 7.13-9.38%, respectively. Similarly, in the case of the FC meta-attribute, after 30 iterations the normalised RMS error and misclassification percentage for both the train and test data sets reached minimum values between 0.3-0.45 and 3.08-7.55%, respectively (Fig. 10f). It is important to attain a minimum error between the test and train data, and thus achieve a closer approximation between the computed (system-generated) and the targeted (based on the interpreter knowledge and skills) outputs. The relative contribution (weights assigned to each input nodes) offered by the input sets (seismic attributes for both the cases) are shown in Tables 2 and 3.

5.5 Enhanced interpretation of hard-linked fault zones and fluid pathways

The TFC meta-attribute highlights subsurface structural features and brings out thinned continuous fault images from the data. The Monganui, Moki and the underlying Tikorangi Formations are structurally deformed, and have been compartmentalised in a series of half-graben structures (Figs. 11). Faults captured by the TFC meta-attribute within the Monganui Formation strike to the NE (Figs. 12). The master fault i.e., the PNF (Fault F3) presents a sigmoidal geometry and divides the formation into eastern and western structural

compartments. The eastern compartment belongs to the hanging-wall domain and the western compartment belongs to the footwall domain.

Towards the NW part of the Monganui Formation, faults exhibit a curved (or semi-circular) geometry, e.g. Fault F1 (Fig. 12b). These curved faults are further associated with several splays with a horse-tail appearance (See Omosanya et al., 2017; Fig. 12b and 13a). A similar geometry is also observed in the central part of the study area at the level of the Monganui Formation, e.g. in Fault F2 (Fig. 12b). The ramps between faults F1-F3 and F2-F3 are hard-linked and breached by several parallel faults and fault splays (Figs. 12b and 13b). Fault F3 is segmented in the northern part of the study area, but a sigmoidal shape is more prominent from the centre of the study area towards the south (Fig. 12c). A Y-shape fault (F4) and associated fault splays are observed in the south (Figs. 12c and 13c). These splays breach the ramp formed between F4 and F3 (Figs. 12c and 13c).

The Moki Formation is also deformed by a complex fault system (Figs. 14). Faults within the Moki Formation have NNE-SSW strikes (Figs. 14). Faults in the northern part of the study area are curved (F1) and parallel along their strike (Fig. 14b). In the southern part, a relay ramp between the sigmoidal F3, Y-shaped F4 and curved F2 is breached by a series of parallel faults (Fig. 14c). Discontinuous structures within the underlying Oligocene Tikorangi unit demonstrate two major fault strikes, i.e. NNE-SSW and NE-SW (Figs. 15). Curved faults (F1 and F2) are prominent and well-developed within this latter unit (Fig. 15a). In addition, the segmented F3 continues to reveal an S-shaped pattern (Figs. 15b-c). The ramps between the faults F1, F2 and F3 are breached by en-enchelon faults (step faults) in the northern to central parts of the seismic volume. The southern part of the study area is deformed by several fault splays with Y-shaped geometries (Fig. 15c).

Relay ramps within the western structural compartment of the Miocene units are deformed internally and, hence, are further breached by faults and minute structural discontinuities (Figs. 13, 14 and 16a). Such intense breaching of the relay ramps provides conductive pathways for fluid migrating towards younger strata (Fig. 16a). The FC meta-attribute captures these leakage pathways where fluids are observed to migrate through the Miocene succession to younger strata through the hard-linked fault zones (Fig. 16b). Breaching of the relay ramps, and fluid leakage through these structures, can be further observed in Fig. 17, where seismic data is sliced at t=2.2 s. In the northern part, the relay ramp between faults F2 and F3 is breached with several parallel faults and smaller structures (Fig. 17b). To the south, the relay ramp between faults F3 and F4 is breached by several fault splays (Fig. 17c). These zones

are associated with high fluid probability, thus, signifying fluid leakage through breached structures (Figs. 17d-f and 18a-b)

6. Discussion

6.1. The TFC and FC: An automated approach of interpretation

We observe that faults F1, F2, F3 and F4 consist of hard-linked relay ramps (Table 4). This geological scenario is prominently elucidated through the automated approach adopted in this work. This automated approach is inspired by a unique rule, where the geological targets are interpreted based on the interpreter's skills and verdict. Based on such facts, all appropriate locations that illustrate the maximum and minimum probability of faults and fluid zones in the seismic data are selected (Figs. 10a and d). The response of multiple seismic attributes adds value during such selection. Once satisfied, the attribute responses and identified locations are trained through a fully connected multilayer perceptron Neural Network so as to minimize errors in interpretation, and an optimal output is obtained (Figs. 10b, c, e and f). In turn, this generated a meta-attribute showing sharper faults, and revealing fluid migration pathways in the interpreted seismic data volume (Figs. 11 and 15).

The TFL attribute is efficient in generating thinned fault images from the data. Its success depends on the number of scans performed such that subsurface structural details are imaged from the data (Hale, 2013). The optimised TFL attribute in the present study illustrates thinned fault images from the seismic volume (Figs. 8 and 19a). However, geological structures in the NE part of the prospect are poorly captured, and lack structural continuity and connectivity. The TFC meta-attribute improves the interpretation by enhancing the presence of geological features in the data (Fig. 19b). Faults observed throughout the Parihaka prospect are now continuous and prominent. Hence, such a process of amalgamating seismic attributes and generating a meta-attribute is by all means superior to single attribute computation.

The efficiency of the TFC is compared in Fig. 20 to individual attributes, e.g. the coherency attribute of Bahorich and Farmer (1995) and Marfurt et al. (1998) and the similarity attribute of Tingdahl and de Groot (2003). At t=1.7s the TFC meta-attribute demonstrates its superiority to the individual seismic attributes. The coherency and similarity attributes show the geometry of faults from the data, but local structural patterns are poorly visible and lack in continuity and connectivity (e.g. the northern zones with a question mark and yellow circle; the southern zones with an orange circle; Figs. 20a and b). The TFC meta-attribute improves the visibility of structures, making structural continuity more prominent (Fig. 20c). Similar observations are made for the time slice t=2.0 s as compared to common seismic attribute analysis used in

Figs. 20d, 20e and 20f. A downside of the TFC and FC meta-attributes lies in the use of noisy data as input for the meta-attribute design. Noisy data will mislead the interpreter and results in the erroneous identification of geological features. Hence, interpreters should start their analysis by excluding noisy areas from the data; if these noisy areas are trained with attribute responses, the learning capability and the generalization efficiency of the Neural Network can be significantly reduced.

6.2 Implications for fluid plumbing through hard-linked faults

Relay ramps typically provide pathways and control the vertical migration of hydrocarbons (Peacock and Parfitt, 2002; Kim et al., 2004; Fossen and Rotevatn, 2016). This setting becomes more favourable when structural complexity within these ramps increases, i.e. when the ramp is breached by faults and fractures. In such a situation, these zones become the loci of a range of fluid-rock interactions, making them economically significant. In the present study, Miocene strata are structurally deformed by a series of hard-linked fault zones. Arco Petroleum (1992) documented the occurrence of hydrocarbon migration from the Pakawau Formation into reservoir intervals in the Monganui, Moki and Urenui Formations (Fig. 3). The FC meta-attribute logically reveals this process where hydrocarbon is observed to migrate through the breached relay ramps, at the level of Miocene strata, into younger sedimentary units. Most of these breached ramps are observed between faults F1 and F2, and between F3 and F4 (Figs. 16, 17 and 18). Though hydrocarbons might have been accumulated within Miocene reservoir units, intense tectonic activity affecting these latter resulted in the breaching of the relay ramps. Most of these breaching events are observed during the Miocene period. Such a breaching resulted in the generation of several leakage zones within the Miocene reservoirs, allowing fluid to migrate further into younger strata. The TFC and FC meta-attributes strengthen this fact and elucidate the location of hydrocarbon leakage zones through hard-linked fault zones.

7. Conclusions

A combination of multiple seismic attributes trained by the interpreters' skills and experience yielded two meta-attributes, the Thinned Fault Cube (TFC) and the Fluid Cube (FC), which provide enhanced images of faults and fluid migration pathways from 3D seismic reflection data. The approach brought out the structural architecture of faults compartmentalising Miocene strata in the Parihaka prospect, New Zealand. Main conclusions of this work are as follows:

a) The workflow adopted in this work was able to identify fluid flow pathways through hard-linked fault zones at Miocene and Pliocene level. The only downside of using

such workflow lies in the use of noisy data as input for the meta-attribute design, a caveat that will lead to the erroneous interpretation of non-geological features.

b) The approach taken to interpret the geological features from seismic reflection data using Neural Networks is not painstaking; rather it is an automated process and makes use the interpreters' skills to produce a reliable interpretation of geological targets.
c) It is worth noting that several new seismic attributes may evolve in the future, and these can be incorporated into the proposed algorithm to further enhance the interpretation.
d) The primary concern of an interpreter should be to consistently improve the imaging capabilities of seismic data such that newer approaches can prominently image subsurface geological targets from the seismic volume.

Acknowledgements

This work is a joint research collaboration of the Seismic Group at CSIR-NGRI, 3D Seismic Lab, Cardiff University and WIHG, Dehradun, India. The authors thank the New Zealand Petroleum & Minerals (NZP&M) for giving permission to access the seismic and borehole information for this research. dGB Earth Sciences is dully acknowledged for providing software support for this work. The authors are thankful to the Editor-in-chief Dr. Masimo Zecchin, section editor Dr. Adam Bumby and reviewer Dr. Xinming Wu, for their constructive comments that have improved the quality of the work. The first author also thanks DST, Govt. of India for providing him with the INSPIRE fellowship.

Appendix A

A sigmoid function is an S-shaped mathematical function or simply a sigmoid curve. Mathematically, it is defined as:

$$y(x) = 1/(1 + e^{-x}) \text{.....(A1)}$$

The derivative of this function is given as

$$\frac{dy}{dx} = \frac{e^x}{(1+e^x)^2} \text{ .....(A2)}$$

The sigmoid function is very often used in neural network to introduce nonlinearity in the neural model. Moreover, it is continuously differentiable which makes the computation easier.

Appendix B

The classification percentage is defined as the ratio of number of correct predictions to the total number of predictions, and is used to judge how best the intelligent neural model is able to differentiate the given distribution into object and non-object classes.

$$Classification\ (\%) = \frac{Number\ of\ correct\ predictions}{Total\ number\ of\ predictions} \times 100 \quad \text{..... (B1)}$$

In turn, the misclassification percentage, is defined as the ratio of number of wrong predictions to that of the total predictions. It is given as:

$$Misclassification\ (\%) = \frac{Number\ of\ wrong\ predictions}{Total\ number\ of\ predictions} \times 100 \quad \text{..... (B2)}$$

Appendix C

The normalised RMS (nRMS) error is computed from the RMS error between the targeted (t_i) (which the interpreter expects) and computed (c_i) (values that the network computes) values for i ranging from 1 to n. This is given by (Aminzadeh and de Groot, 2006):

$$RMS = \sqrt{\frac{1}{n}} \sum_{i=1}^{n} (t_i - c_i)^2 \quad \text{..... (C1)}$$

and,

$$normalized\ RMS = RMS \Big/ \sqrt{\frac{1}{n}} \sum_{i=1}^{n} (t_i - mean)^2 \text{ .....(C2)}$$

where, the mean is given by:

$$mean = \frac{1}{n} \sum_{i=1}^{n} t_i \text{ ..... (C3)}$$

Appendix D

Similarity quantifies how similar are the two segments of seismic traces $u(x, y, t)$ (Tingdahl, 2003). Considering two trace segments (x_A,y_A) and (x_B,y_B), centered at a time t, the similarity (*S*) between these two trace segments (Tingdahl, 2003; Tingdahl and de Rooij, 2005) is expressed as**:**

$$S = 1 - \frac{|a-b|}{|a|+|b|} \quad \text{..... (D1)}$$

where:

$$a = \begin{bmatrix} u(x_A, y_A, t + t_1) \\ u(x_A, y_A, t + t_1 + dt) \\ \cdots \\ u(x_A, y_A, t + t_2 - dt) \\ u(x_A, y_A, t + t_2) \end{bmatrix}, b = \begin{bmatrix} u(x_B, y_B, t + t_1) \\ u(x_B, y_B, t + t_1 + dt) \\ \cdots \\ u(x_B, y_B, t + t_2 - dt) \\ u(x_B, y_B, t + t_2) \end{bmatrix}$$

In these equations dt is the sampling interval, t_1 is the relative start time of the comparison window, t_2 is the relative stop-time of the comparison window, and u is the amplitude value in seismic cube. The output of the similarity attribute is enhanced, when computation is made using dip-steering as an input. The output in this case is called as dip-steered similarity. The dip-steered similarity is expressed as (Tingdahl, 2003):

$$\mathrm{S_{dip}} = 1 - \frac{|\mathrm{a_{dip}} - \mathrm{b_{dip}}|}{|\mathrm{a_{dip}}| + |\mathrm{b_{dip}}|} \quad \text{..... (D2)}$$

where:

$$a_{dip} = \begin{bmatrix} u(x_A, y_A, t_A + t_1) \\ u(x_A, y_A, t_A + t_1 + dt) \\ \cdots \\ u(x_A, y_A, t_A + t_2 - dt) \\ u(x_A, y_A, t_A + t_2) \end{bmatrix}, b_{dip} = \begin{bmatrix} u(x_B, y_B, t_B + t_1) \\ u(x_B, y_B, t_B + t_1 + dt) \\ \cdots \\ u(x_B, y_B, t_B + t_2 - dt) \\ u(x_B, y_B, t_B + t_2) \end{bmatrix}$$

t_A and t_B are the dip-steered times going from the position (x, y, t) to the traces at (x_A,y_A) and (x_B,y_B), respectively, and *u* is the amplitude value in the seismic cube.

Appendix E

The Ridge Enhancement Filter (REF) is computed by extracting nine (9) similarity values surrounding the central evaluation point. This is done by scanning the target in four different directions (Fig. E.1a), i.e. the inline, the xline and two diagonals oriented in 45 and 135 degrees in a time slice domain of the similarity attribute volume (Brouwer and Huck, 2011). Let us consider the Fault F1 as shown in the Fig. E.1b. AB and CD are two segments crossing the faults. The central evaluation point is shown through a blue transparent circle.

Thus, the REF is defined by the following equation:

$$REF = \frac{Sum\ of\ values\ on\ either\ side\ of\ the\ fault}{2} - central\ value \quad \text{.....E1}$$

Either side of the fault will compute small values for the REF, whereas the places over the fault are associated with large ridge values. The REF attribute improves fault visibility by sharpening the edges, while maintaining the connectivity of the fault networks.

Appendix F

The Thin Fault Likelihood (TFL) attribute aims to compute sharp fault images from seismic data (Hale, 2013). The computation uses the principle of fault-oriented semblance. Using the reflection slopes, initially a structure-oriented semblance is computed. This is expressed as:

$$semblance = \frac{\langle image \rangle_s^2}{\langle image^2 \rangle_s} \quad \text{.....(F1)}$$

where a structure-oriented averaging $\langle \cdot \rangle_s$ operation is performed. Such computation results in large semblance values for small numerators and denominators. These variations can be reduced by additional smoothing of the numerators and denominators. When incorporating this additional smoothing, the semblance ratio can be defined as:

$$semblance = \frac{\langle \langle image \rangle_s^2 \rangle_f}{\langle \langle image^2 \rangle_s \rangle_f} \quad \text{..... (F2)}$$

where $\langle \cdot \rangle_f$ denotes the additional smoothing.

After applying such smoothing, the fault likelihood attribute is defined as:

$$f \equiv 1 - (semblance)^8 \quad \text{.....(F3)}$$

The power term used in the above equation, helps to discriminate between the samples corresponding to larger and smaller likelihoods of fault. The computation of f becomes accurate if some prior information on fault orientation and locations are available. Scanning the numerator and denominator (Eq. F2) in the direction of fault strikes and dips help the accurate alignment of structures in their respective orientations, and improves the imaging of structures in seismic data (Hale, 2013). The TFL output values range from 0 to 1, where 0 refers to the minimum likelihood of faults, and 1 refers to maximum likelihood of faults.

Appendix G

The Average Frequency Squared (AFS) attribute helps revealing the responses pertaining to loss in frequency components in faults and within disordered fluid zones. The AFS can mathematically be expressed as (Tingdahl and de Rooij, 2005):

$$\mathrm{AFS} = (\sum_{i=1}^{N} p(\omega_i)^2\, \omega_i^2)/(\sum_{i=1}^{N} p(\omega_i)^2) \quad \text{.....(G1)}$$

where, $p(\omega)$ is the complex response of the trace segments in the Fourier domain and N is the length of the signal.

Appendix H

The Energy attribute at (x, y, t) is defined as the sum of the squared amplitudes within a given window (Tingdahl, 2003), and is given by:

$$E = \sum_{\tau=t_1}^{t_2} u(x, y, t+\tau)^2 \quad \text{..... (H1)}$$

where, t_1 and t_2 are the relative start and stop times of the energy window. Fluid zones are outlined as low amplitude and low energy disturbed events.

References

Arco Petroleum, 1992. Arawa-1 Final well report, *PPL 38447*, Ministry of Economic Development New Zealand: Unpublished Petroleum Report Series *PR 1824*, 1–463.

Aminzadeh, F. and de Groot, P., 2006. An Introduction to Artificial Neural Networks. In: Neural networks and other soft computing techniques with applications in the oil industry: EAGE Publications, Netherlands, 13-35.

Aydin, A., Borja, R.I., Eichhubl, P., 2006. Geological and mathematical framework for failure modes in granular rock. J. Struct. Geol., 28, 83–98.

Alarfaj, M., Lawton, D. C., 2012. Interpreting fault-related gas leakage. CREWES Research Report, 24, 1-10.

Bahorich, M., Farmer, S., 1995. 3-D seismic discontinuity for faults and stratigraphic features: The coherence cube. Lead. Edge., 14. 1053-1058.

Bense, V. F., Baalen, R. V., 2004. The effect of fault relay and clay smearing on groundwater flow patterns in the Lower Rhine Embayment. Basin Res., 16, 397-411.

Breit, G.N., Meunier, J., 1990. Fluid inclusion, d18O, and 87Sr/86Sr evidence for the origin of fault-controlled copper mineralization, Lisbon Valley, Utah, and Slick Rock District, Colorado. Econ. Geol., 85, 884–891.

Brouwer, F., Huck, A., 2011. An integrated workflow to optimize discontinuity attributes for the imaging of faults, in Proceedings: Attributes: New Views on Seismic Imaging—Their Use in Exploration and Production, GCSSEPM, 31st Annual Conference. 496-533.

Chenrai, P., Huuse, M., 2017. Pockmark formation by pore water expulsion during rapid progradation in the offshore Taranaki Basin, New Zealand. Mar. Pet. Geol., 82, 399-413.

Chopra, S., Marfurt, K. J., 2007. Seismic attributes for prospect identification and reservoir characterization. SEG, Tulsa.

Cohen, I., Coult, N., Vassiliou, A. A., 2006. Detection and extraction of fault surfaces in 3D seismic data. Geophy., 71, 4, P21-P27

Curewitz, D., Karson, J.A., 1997.Structural settings of hydrothermal out flow: fracture permeability maintained by fault propagation and interaction. J. Volcanol. Geotherm. Res., 79, 149–168.

Cybenko, G. 1989. Approximation by superpositions of sigmoidal functions. Math. Control Signals Syst., 2, 303-314.

Dini, D.S.W., Innocenti, F., Rocchi, S., 2008. Magma emplacement in a transfer zone: the Miocene mafic Orano dyke swarm of Elba Island, Tuscany, Italy. Geolo. Soc. of London, Spec. Pub., 302, 131–148.

Dockrill, B., Shipton, Z. K., 2010. Structural controls on leakage from a natural CO_2 geologic storage site: Central Utah, USA, J. Struct. Geol., 32.

Ferrill, D.A., Morris, A.P., 2001. Displacement gradient and deformation in normal fault systems. J. Struct. Geol., 23, 619–638.

Fossen, H., Johansen, T.E.S., Hesthammer, J., Rotevatn, A., 2005. Fault interaction in porous sandstone and implications for reservoir management; examples from Southern Utah. AAPG Bulletin, 89, 1593–1606.

Fossen, H., Schultz, R.A., Shipton, Z.K., Mair, K., 2007. Deformation bands in sandstone—a review. Geol. Soc. of London, 164, 755–769.

Gartrell, A., Zhang, Y., Lisk, M., Dewhurst, D., 2004. Fault intersections as critical hydrocarbon leakage zones: integrated field study and numerical modelling of an example from the Timor Sea, Australia. Mar. Petrol. Geol., 21, 1165–1179.

Giba, M., Nicol, A., Walsh, J. J., 2010. Evolution of faulting and volcanism in a back-arc basin and its implication for subduction processes. Tectonics, 29, 4, TC4020, 1-18.

Giba, M., Walsh, J. J., Nicol, A., 2012. Segmentation and growth of an obliquely reactivated normal fault. J. Struct. Geol., 39, 259-269.

Gürboğa, Ş., 2014. Structural analyses of Şaphane relay ramps and fault linkage evolution in active extensional regime, western Turkey. Turk. J. Earth Sci., 23, 615-626.

Kim, Y.-S., Peacock, D.C.P., Sanderson, D.J., 2004. Fault damage zones. J. Struct. Geol., 26, 503–517

Kristensen, M.B., Childs, C., Olesen, N.Ø., Korstgård, J.A., 2013. The microstructure and internal architecture of shear bands in sand–clay sequences. J. Struct. Geol., 46,129–141.

Kristiansen, K., 2011. Vertical fault leakage in the western part of the Hammerfest Basin. Unpublished MSc thesis, University of Bergen, (94 pp)

Knox, G.J., 1982. Taranaki Basin, structural style and tectonic setting. N. Z. J. Geol. Geophy., 25, 125-140.

Pilaar, W. F. H., Wakefield, L. L. 1978. Structural and stratigraphic evolution of the Taranaki Basin, offshore North Island, New Zealand. J. Aus. Pet. Explor. Asso., 18, 93–101.

Fossen, H., Rotevatn, A., 2016. Fault linkage and relay structures in extensional settings-A review. Earth Sci. Rev., 154, 14-28.

Hale, D., 2013. Methods to compute fault images, extract fault surfaces and estimate fault throws from 3D seismic images. Geophysics, 78, 2, O33-O43.

Hinton, G. E., Osindero, S., Teh, Y. W., 2006. A Fast Learning Algorithm for Deep Belief Nets. Neural. Comput., 18, 1527-1554.

Höcker, C., Fehmers, G., 2002. Fast structural interpretation with structure-oriented filtering. Lead. Edge., 21, 238-243.

Hornik, K., 1991. Approximation Capabilities of Multilayer Feedforward Networks. Neural Net., 4, 251-257.

Higgs, K.E., King, P. R., Raine, J. I., Sykes, R., Browne, G. H., Crouch, E. M., Baur, J. R., 2012. Sequence stratigraphy and controls on reservoir sandstone distribution in an Eocene marginal marine-coastal plain fairway, Taranaki Basin, New Zealand. Mar. Pet. Geol., 32, 110-137.

Huang, L., Dong, X., Clee, T. E., 2017. A scalable deep learning platform for identifying geologic features from seismic attributes. Leading Edge, 36, 249-256.

Iacopini, D., Butler, R. W., 2011. Imaging deformation in submarine thrust belts using seismic attributes. Earth Planet. Sci. Lett., 302, 414-422.

Iacopini, D., Butler R. W., Purves S., McArdle N., De Freslon N., 2016. Exploring the seismic expression of fault zones in 3D seismic volumes. J. Struct. Geol., 89, 54-73.

Jaglan, H., Qayyum, F., Huck, H., 2015. Unconventional seismic attributes for fracture characterization, First Break, 33, 101-109.

King, P.R., Thrasher, G. P., 1996. Cretaceous-Cenozoic geology and petroleum systems of the Taranaki Basin, New Zealand: Institute of geological and Nuclear Sciences, Lower Hutt (N.Z.) Monograph 13.

King, P.R., Naish, T. R., Browne G. H., Field, B. D., Edbrooke, S. W., 1999. Cretaceous to Recent sedimentary patterns in New Zealand, Folio Series 1. Lower Hutt, Institute of Geological and Nuclear Sciences.

King, P.R., 2000. Tectonic reconstructions of New Zealand 40Ma to the present. N. Z. J. Geol. Geophy., 43, 611-638.

Kumar, P. C., 2016. Application of geometric attributes for interpreting faults from seismic data: an example from Taranaki Basin, New Zealand. SEG Technical Program Expanded Abstract, 2077-2081.

Kumar, P. C., Mandal, A., 2017. Enhancement of fault interpretation using multi-attribute analysis and artificial neural network (ANN) approach: a case study from Taranaki Basin, New Zealand. Explor. Geophy., 49, 409-424.

Kumar, P. C., Sain, K., 2018. Attribute amalgamation-aiding interpretation of faults from seismic data: An example from Waitara 3D prospect in Taranaki basin off New Zealand. J. App. Geophy., 159, 52-68.

Kumar, P. C., Omosanya, K.O, Sain, K., 2019a. Sill Cube: An automated approach for the interpretation of magmatic sill complexes on seismic reflection data. Mar. Pet. Geol., 100, 60-84.

Kumar, P. C., Sain, K., Mandal, A., 2019b. Attribute amalgamation-aiding interpretation of faults from seismic data: An example from Waitara 3D prospect in Taranaki basin off New Zealand. J. App. Geophy., 159, 52-68.

Larsen, P.-H., 1988. Relay structures in a Lower Permian basement-involved extension system, East Greenland. J. Struct. Geol., 10, 3–8

Lu, P., Morris, M., Brazell, S., Comiskey, C., Xiao, Y., 2018. Using generative adversarial networks to improve deep-learning fault interpretation networks. Leading Edge, 37, 8, 578-583.

Manzocchi, T., Health, A.E., Palananthakumar, B., Childs, C., Walsh, J. J., 2008. Faults in conventional flow simulation models: a consideration of representational assumptions and geological uncertainties. Pet. Geosci., 14, 91-110.

Meldahl, P., Najjar, N., Oldenziel-Dijkstra, T., Ligtenberg, H., 2002. Semi-Automated Detection of 4D Anomalies. Paper presented at 64th EAGE Conference & Exhibition.

Mohammedyasin, M.S., Deep-seated faults and hydrocarbon leakage in Snøhvit Gas Field, Hammerfest Basin, southwestern Barents Sea. Master's Thesis, NTNU.

Omosanya, K.O., Johansen, S.E., Eruteya, O.E., Waldmann, N., 2017. Forced folding and complex overburden deformation associated with magmatic intrusion in the Vøring Basin, offshore Norway. Tectonophy., 706, 14-34.

Palmer, J. A., Andrews, P. R., 1993. Cretaceous-Tertiary sedimentation and implied tectonic controls on structural evolution of Taranaki Basin, New Zealand. In: South Pacific Sedimentary Basins: Sedimentary Basins of the world, 2, 309-328, Elsevier, Amsterdam.

Peacock, D.C.P., Sanderson, D.J., 1991. Displacements, segment linkage and relay ramps in normal fault zones. J. Struct. Geol., 13, 721–733.

Peacock, D.C.P., Sanderson, D.J., 1994. Geometry and development of relay ramps in normal fault systems. AAPG Bulletin, 78, 147-165

Peacock, D.C.P, Knipe, R. J., Sanderson, D. J., 2000. Glossary of normal faults. J. Struct. Geol., 22, 291-305.

Peacock, D.C.P., Parfitt, E.A., 2002. Active relay ramps and normal fault propagation on Kilauea Volcano, Hawaii. J. Struct. Geol., 24, 729–742.

Pedersen, S. I., Randen, T., Sonneland, L., Steen, Ø., 2002. Automatic fault extraction using artificial ants: 72nd Annual International Meeting, SEG, Expanded Abstracts, 512-515.

Pedersen, S. I., Skov, T., Hetlelid, A., Fayemendy, P., Randen, T., Sønneland, L., 2003. New paradigm of fault interpretation: 73rd Annual International Meeting, SEG, Expanded Abstracts, 350-353.

Pollard, D.D., Aydin, A., 1984. Propagation and linkage of oceanic ridge segments. J. Geophy. Res., 89, 10017-10028.

Poulton, M. M., 2001. Computational neural networks for geophysical data processing. Vol. 30, Elsevier.

Roberts, A., 2001. Curvature attributes and their application to 3-D interpreted horizons. First Break. 19, 85-100.

Rowland, J.V., Sibson, R.H., 2004. Structural controls on hydrothermal flow in a segmented rift system, Taupo Volcanic Zone, New Zealand. Geofluids 4, 259–283.

Rotevatn, A., Fossen, H., Hesthammer, J., 2007. Are relay ramps conduits for fluid flow? Structural analysis of a relay ramp in Arches National Park., Utah. Geol. Soc. of London, Spec. Pub., 270, 55-71.

Singh, D., Kumar, P.C., Sain K., 2016. Interpretation of gas chimney from seismic data using artificial neural network: A study from Maari 3D prospect in the Taranaki basin, New Zealand, J. Nat. Gas Sci. and Eng., 36, 339-357.

Shaw, J. H., Connors, C., Suppe, J., 2005. Seismic Interpretation of Contractional Fault-Related Folds. In: Seismic Atlas Studies in Geology, 53, AAPG Bulletin.

Sibson, R.H., 1996. Structural permeability of fluid-driven fault-fracture meshes. J. Struct. Geol., 18, 1031–1042.

Tingdahl, K. M., 1999. Improving seismic detectability using intrinsic directionality: Tech. Rep., B194, Earth Sciences Centre, Goteborg University.

Tingdahl, K. M., de Groot, P. F., 2003. Post-stack dip and azimuth processing. J. Seis. Explo., 12, 113-126.

Tingdahl, K. M., 2003. Improving seismic chimney detection using directional attributes. In: Soft Computing and Intelligent Data Analysis in Oil Exploration, vol. 51, edited by Nikarvesh, M., Aminzadeh, F. and Zadeh, L.A, Developments in Petroleum science, pp. 157-173.

Tingdahl, K. M., de Rooij, M., 2005. Semi-automatic detection of faults in 3D seismic data, Geophys. Prospect., 53, 533-542.

Western Geco, 2012. Parihaka 3D PSTM Processing report. Ministry of Economic Development New Zealand: Unpublished Petroleum Report Series *PR4582,* 1–135.

Wu, X., Hale, D., 2016, 3D seismic image processing for faults. Geophy., 81, 2, IM1-IM11.

Wu, X., Fomel, S., 2018a. Automatic fault interpretation with optimal surface voting. Geophy., 83, 5, O67-O82.

Wu, X., Gao, Z., 2019. Detecting faults and channels while enhancing seismic structural and stratigraphic features. Interpretation, 7, 1, T155-T166.

Wu, X., Liang, L., Shi, Y., Fomel, S., 2019b. FaultSeg3D: using synthetic data sets to train an end-to-end convolutional neural network for 3D seismic fault segmentation. Geophy., 84, 3, 1-36.

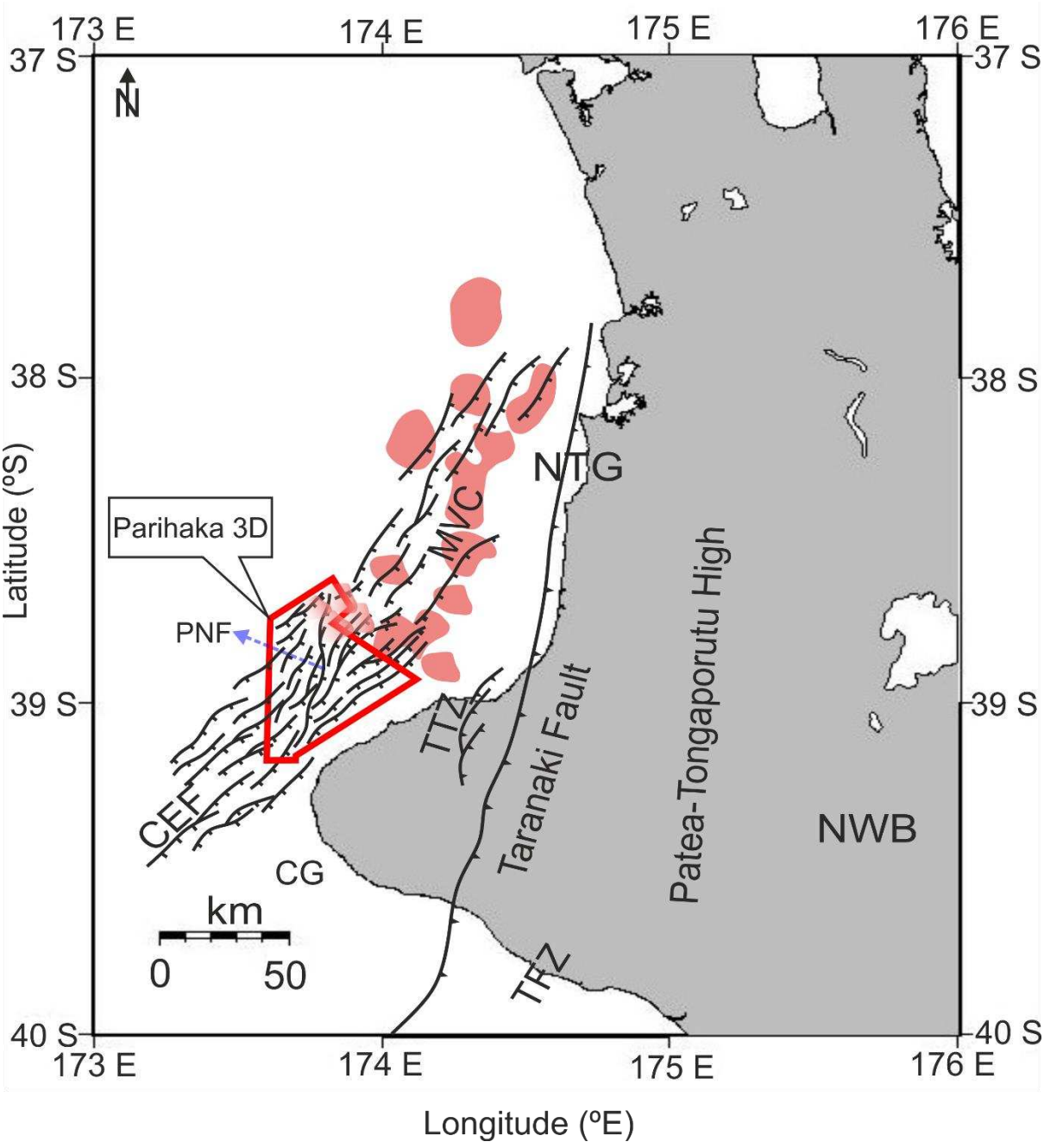

Fig. 1: Location of the Parihaka prospect offshore northern Taranaki Basin, New Zealand. The prospect is crossed by multiple extensional faults trending NE-SW. To the NE, the Parihaka prospect is surrounded by buried intrusive bodies forming the Mohakatino Volcanic Centre (MVC). PNF: Parihaka Normal Fault; NTG: Northern Taranaki Graben; CG: Central Graben; TTZ: Tarata Thrust Zone; NWB: Northern Wanganui Basin; TFZ: Taranaki fault Zone.

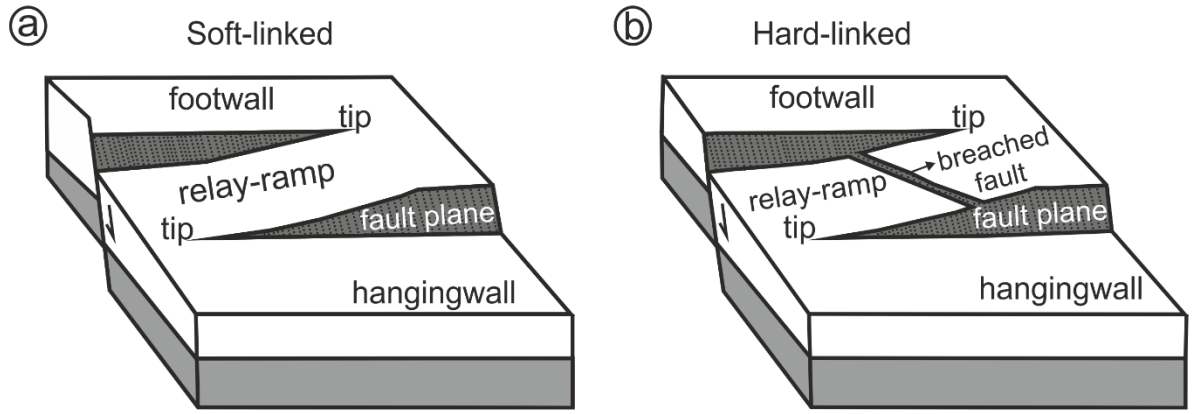

Fig.2: Block diagrams of soft- and hard-linked faults. (a) When the relay ramp is formed between two normal faults the zone is said to be 'soft-linked'. (b) When the relay-ramp is breached by other faults and minute structures the fault system is considered to be 'hard-linked' (after Larsen, 1988; Peacock and Sanderson, 1991, 1994; Gürboğa, 2014).

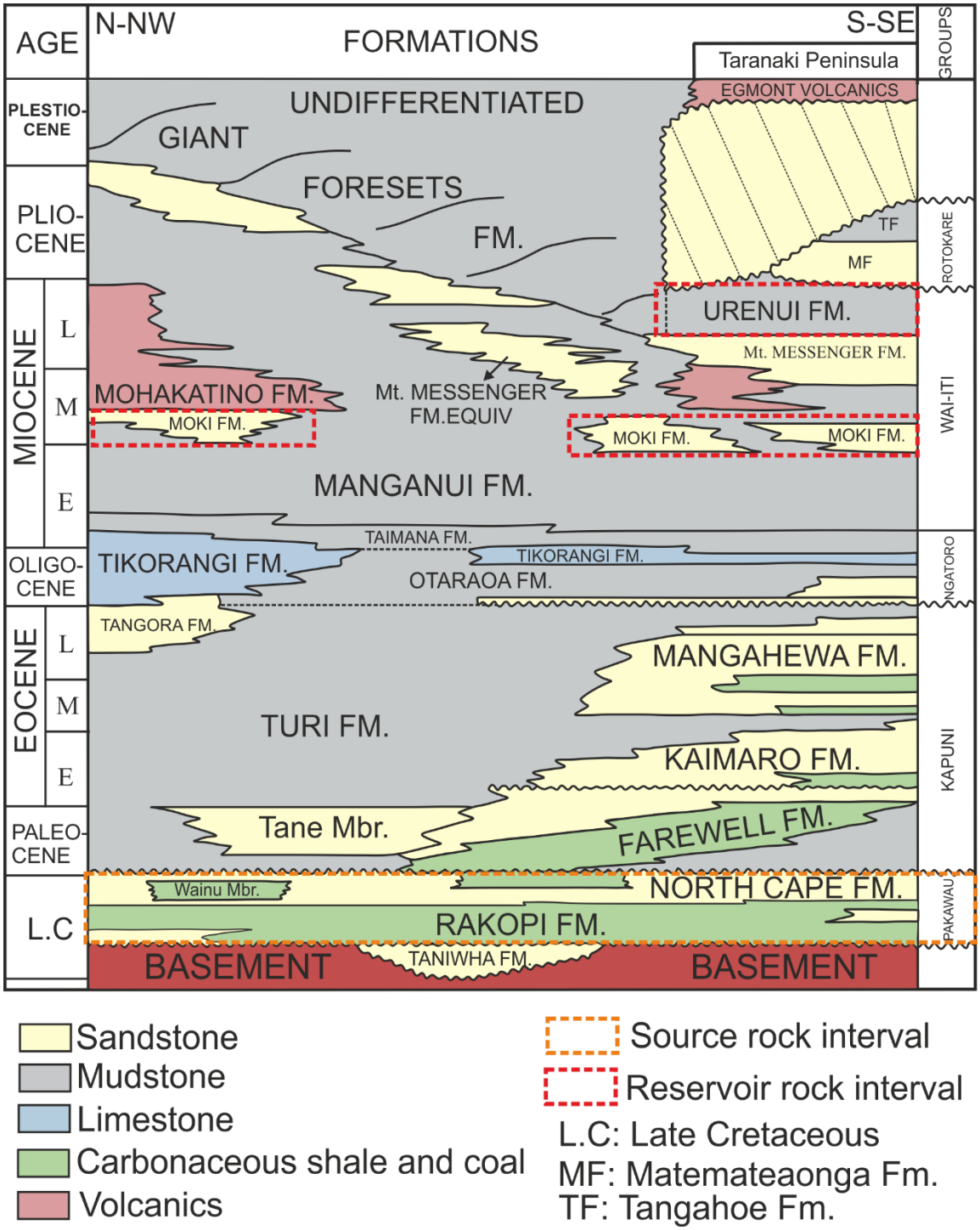

Fig. 3: Lithostratigraphy of the offshore Taranaki basin, New Zealand. Modified after King and Thrasher (1996) and Singh et al. (2016).

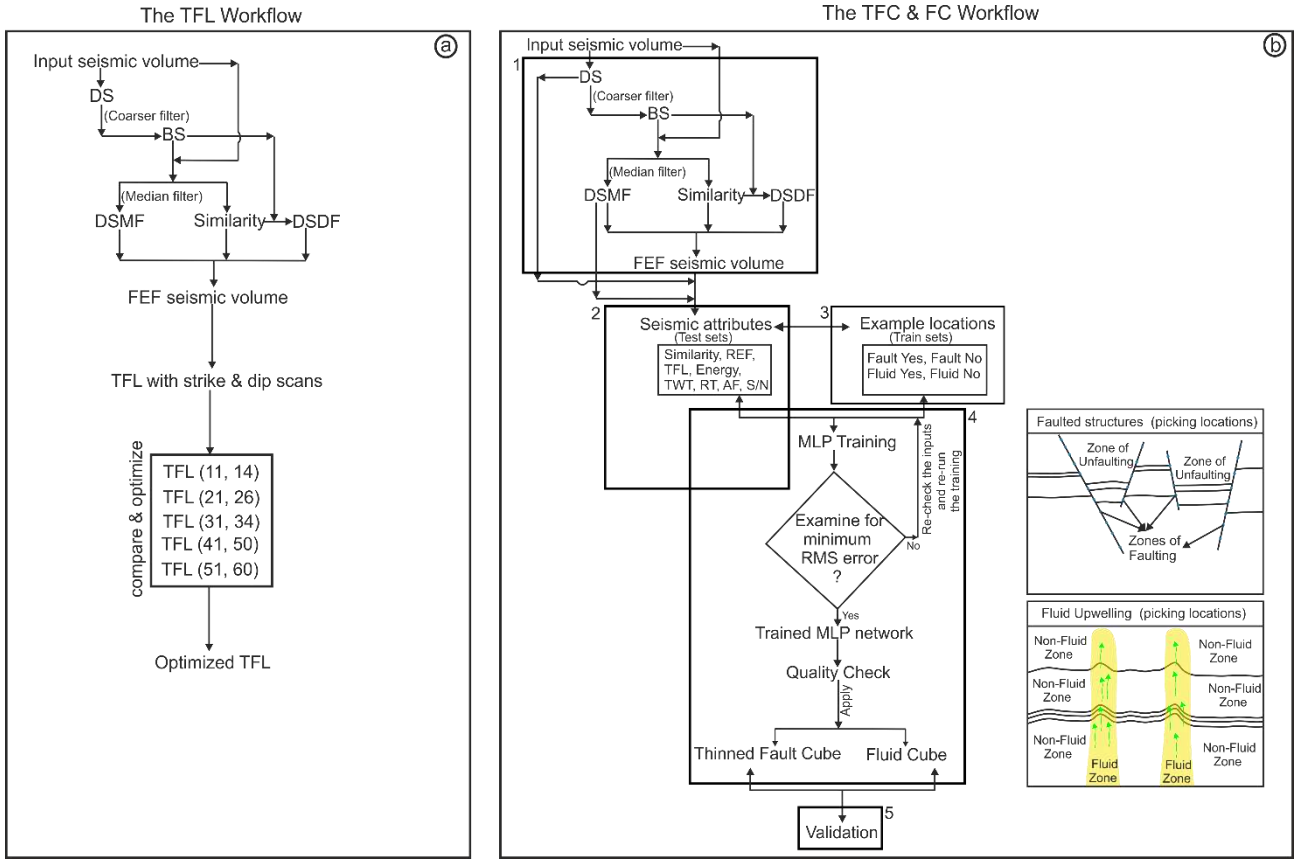

Fig. 4: (a) Proposed workflow for the computation of the Thin Fault Likelihood (TFL). (b) Proposed workflow for the computation of the Thinned Fault Cube (TFC) and Fluid Cube (FC), comprising five main stages: data conditioning (stage 1), preparation of test data sets (stage 2), preparation of train data sets (stage 3), designing and operation of the Neural Network (stage 4) and validation (stage 5). DS: Detailed Steering; BS: Background Steering; DSMF: Dip Steered Median Filter; DSDF: Dip Steered Diffusion Filter; FEF: Fault Enhancement Filter; TFL: Thinned Fault Likelihood; REF: Ridge Enhancement Filter; TWT: Two-way Time; RT: Reference Time; AF: Average Frequency; S/N: Signal to Noise.

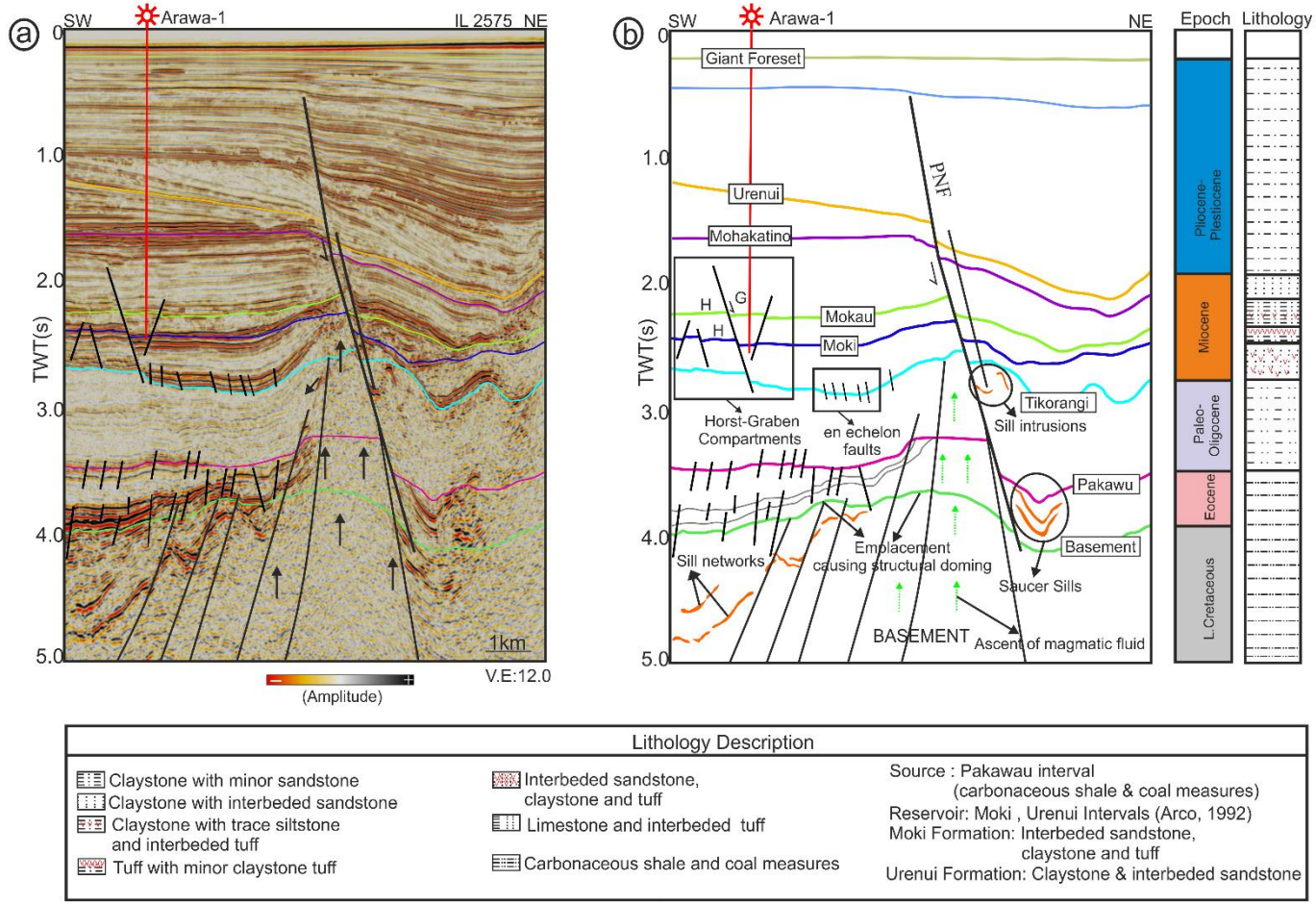

Fig. 5: (a) Uninterpreted seismic line (IL 2575) and (b) corresponding interpretation of seismic line (IL 2575) demonstrating the subsurface structure of the Parihaka prospect. The prospect was drilled by well Arawa-1, which terminates within Miocene strata. The Parihaka Normal Fault (PNF) divides the subsurface strata into two major structural units, the eastern and western compartments. The eastern compartment is further compartmentalised by fault systems. The Miocene Formations (Mohakatino, Mokau and Moki) are associated with horst and graben structures. Furthermore, the basement is intruded by sill complexes from which hydrothermal fluid migrate into younger strata.

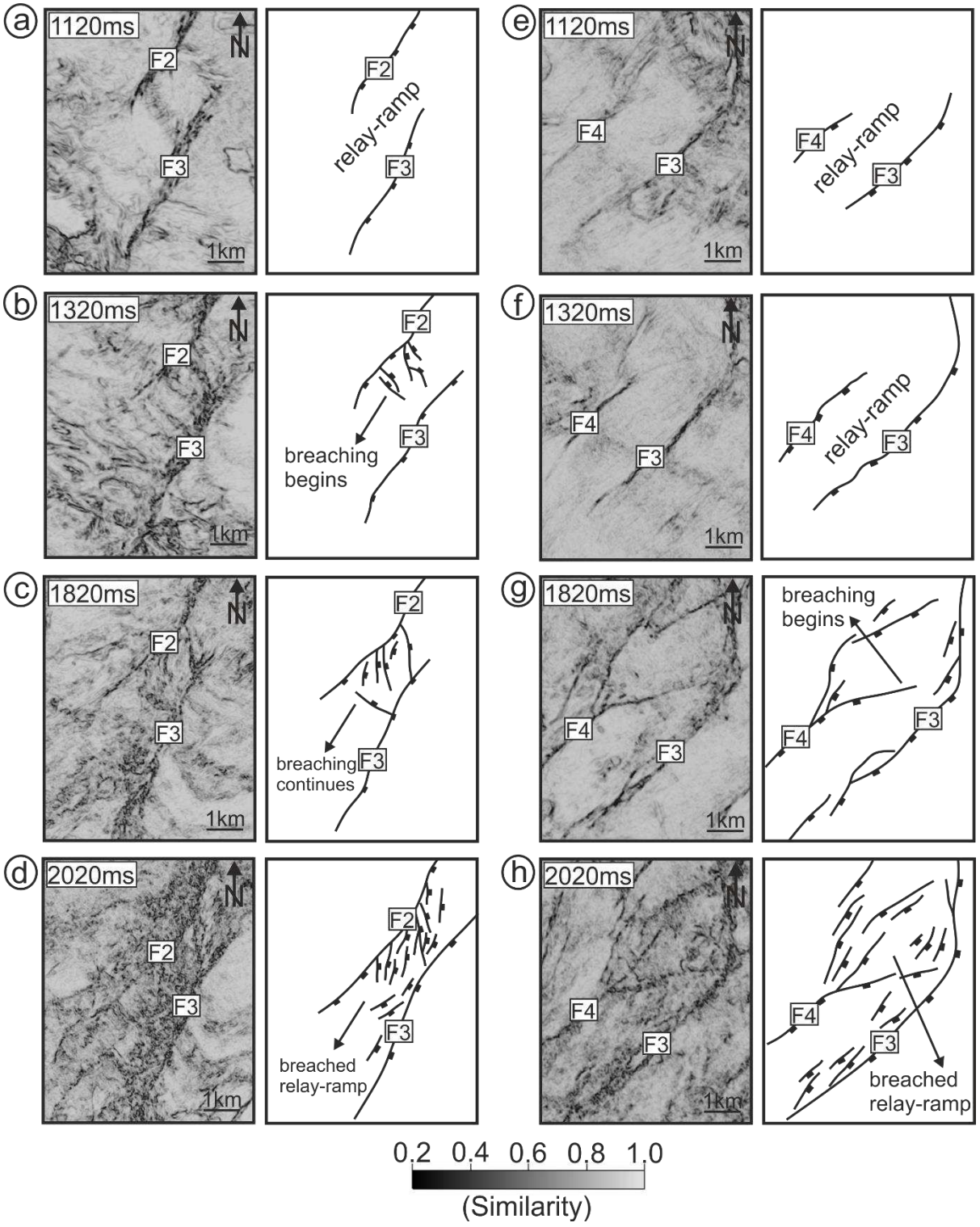

Fig. 6: Breaching of the relay ramp at different depths within the Parihaka prospect as revealed by the similarity attribute. The ramp between two sets of faults F2-F3 and F4-F3 is breached by several faults and minute discontinuous structures. The breaching begins at 1320 ms and becomes predominant at 2020 ms.

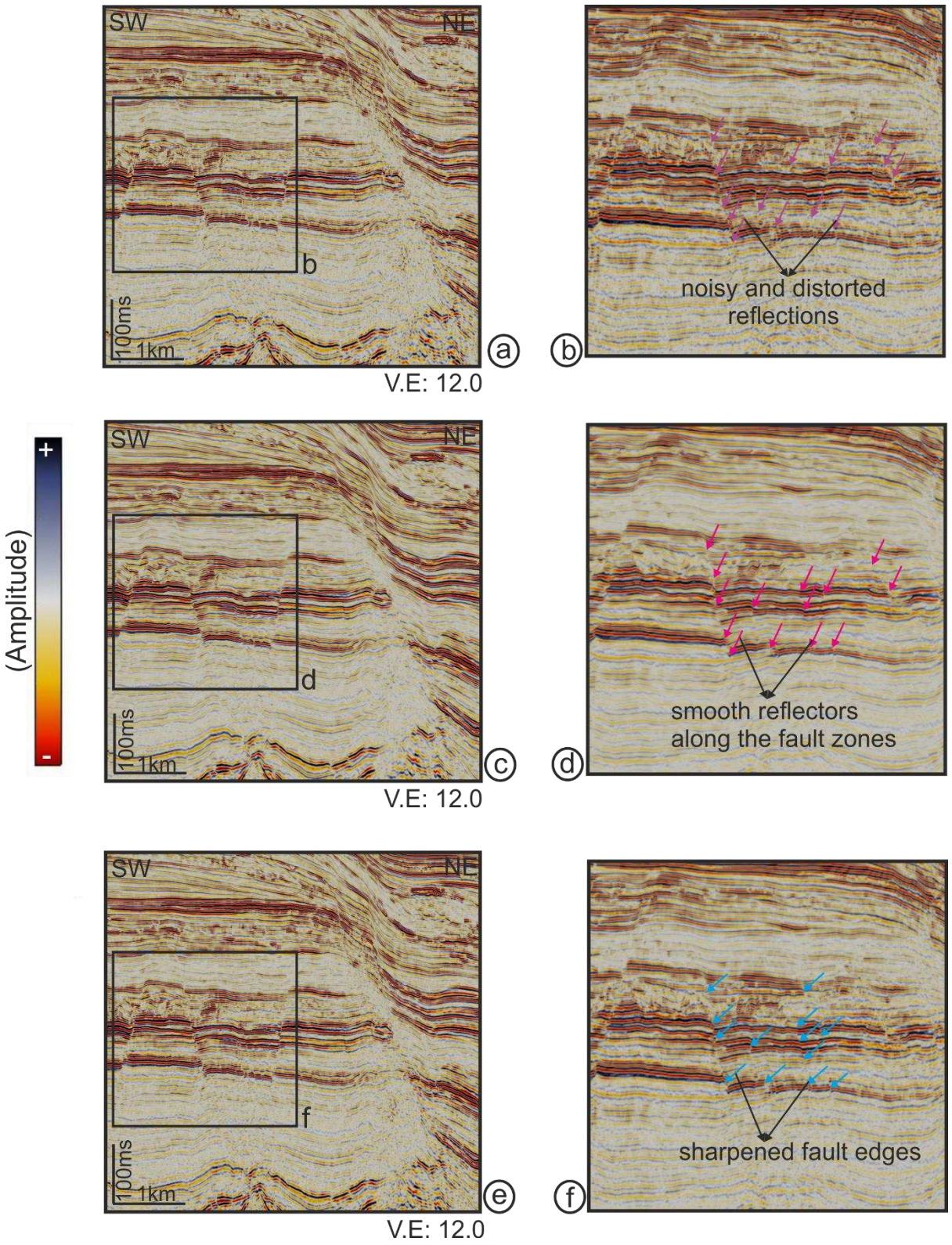

Fig. 7: (a) & (b) Original time migrated seismic section inline (IL) 2231 from the Parihaka prospect. The fault zones shoow noisy and distorted reflections (highlighted in the zoomed right panel). (c) & (d) The Dip Steered Median Filtered (DSMF) conditioned seismic section for the same inline demonstrating improved seismic signal within the fault zones, free from distortion; (e) & (f) The Fault Enhanced Filtered (FEF) sharpens the fault edges and enhances the fault zones as shown in the zoomed panel to the right.

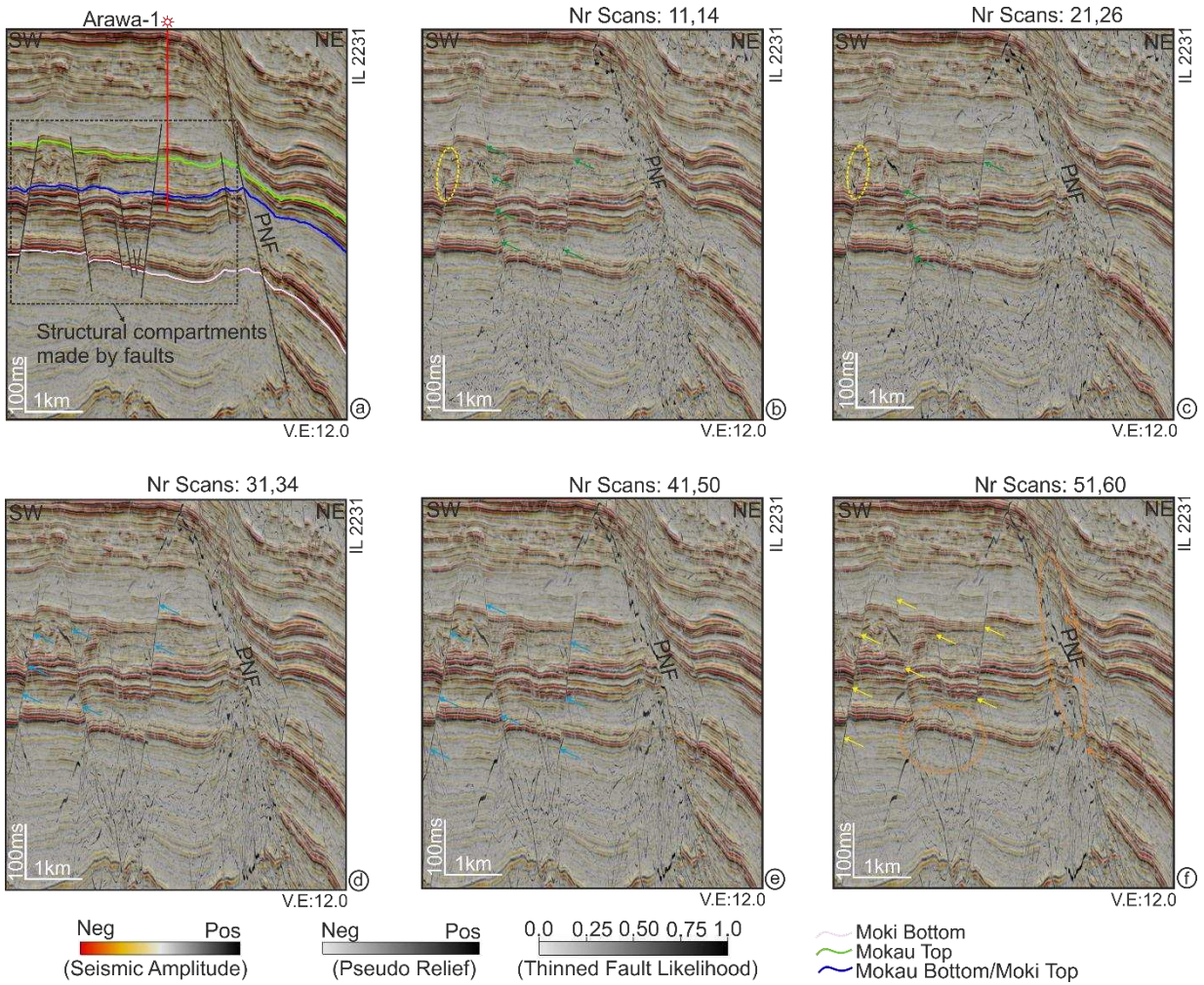

Fig. 8: Thinned Fault Likelihood (TFL) attribute computed for different scans (b-f) along the strike and dip orientations of faults. Scans (b-c) fail to highlight discontinuities at different places of the seismic section. Discontinuities towards the south are poorly imaged (yellow dotted oval and green arrows). A steady improvement is observed for scans (d) and (e). Faults in the northern, central and southern part are clearly visible (cream arrows). Small discontinuities are also observed in deeper strata. Further scanning in (f) brings out most structural discontinuities (yellow arrows and orange dotted oval) and captures maximum structural detail.

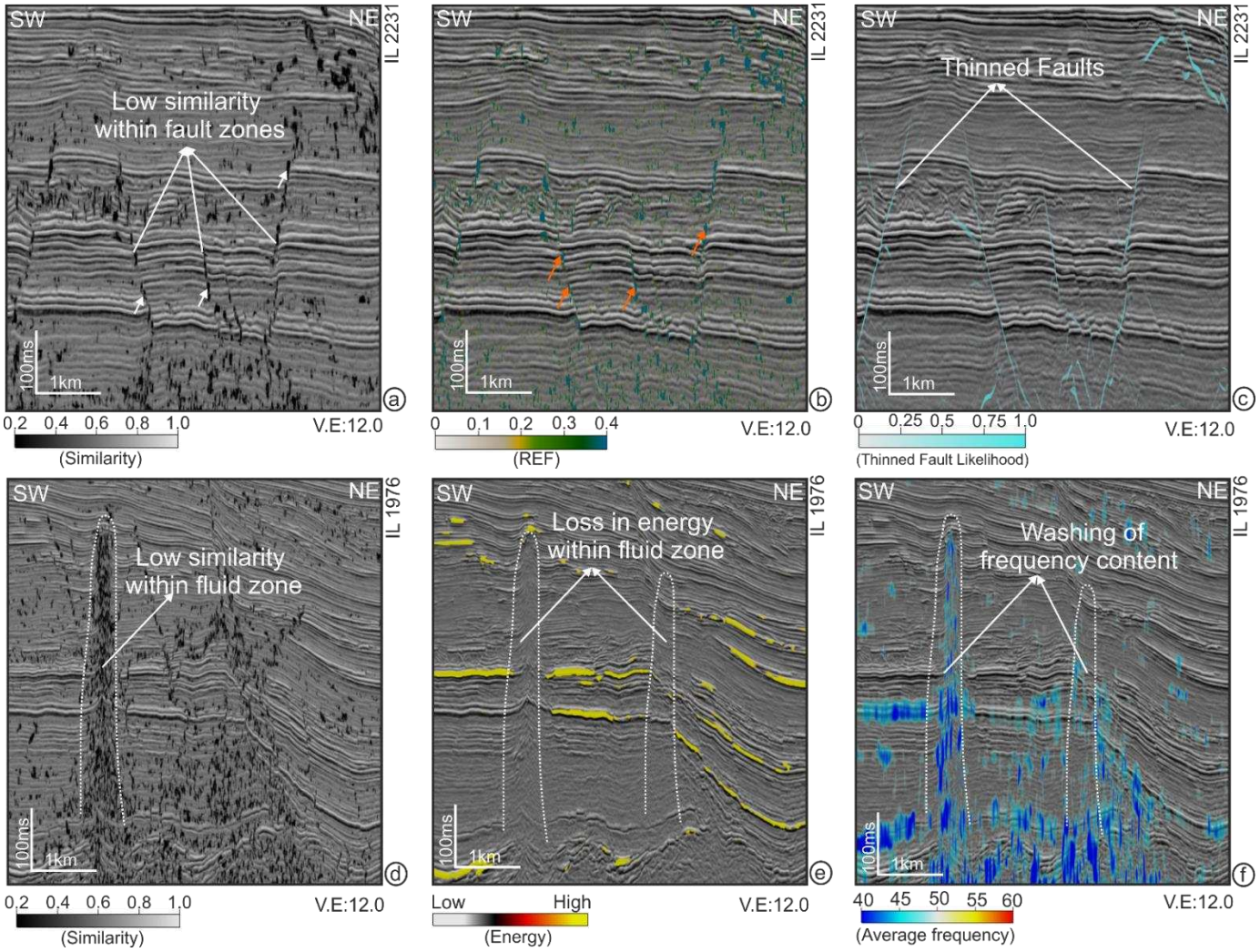

Fig. 9: (a), (b) &(c) Similarity (low similar values), Ridge Enhancement Filter (REF) (high ridges) and TFL (maximum likelihood of structural disturbance) attributes capture the structural signatures of geological discontinuities in the seismic data; (d), (e) & (f) Similarity, Energy and Average Frequency attributes captures the dissimilar, chaotic and frequency 'wash-out' characters of fluid migration zones.

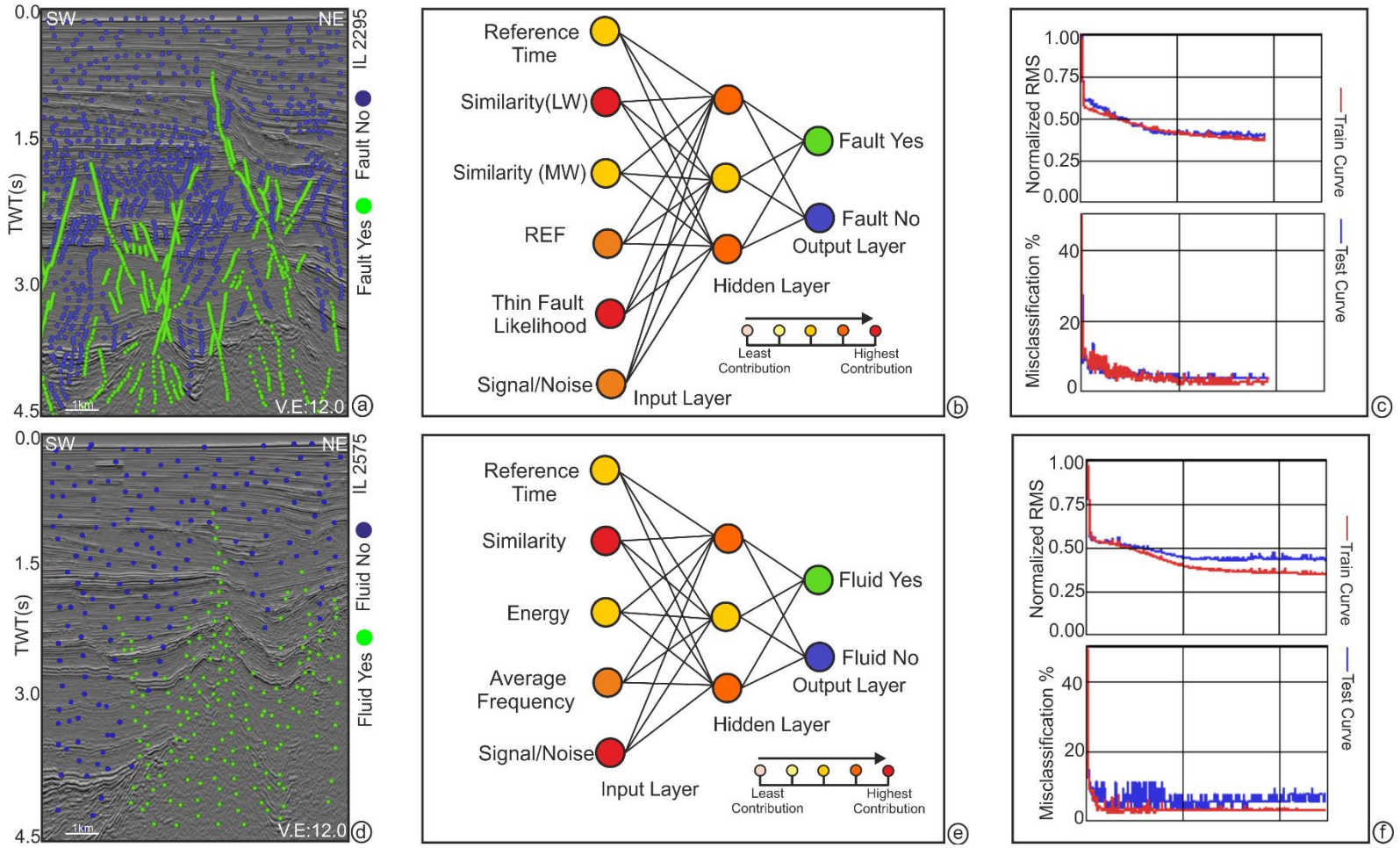

Fig. 10: (a) Example locations showing Fault-Yes and Fault-No; (b) Fully connected multilayer perceptron (MLP) network used for neural operation; (c) Performance evaluation of the Neural Network used to construct the TFC meta-attribute; (d) Example locations showing Fluid-Yes and Fluid-No; (e) Fully connected multilayer perceptron (MLP) network used for neural operation; (f) Performance evaluation of the network for constructing the FC meta-attribute.

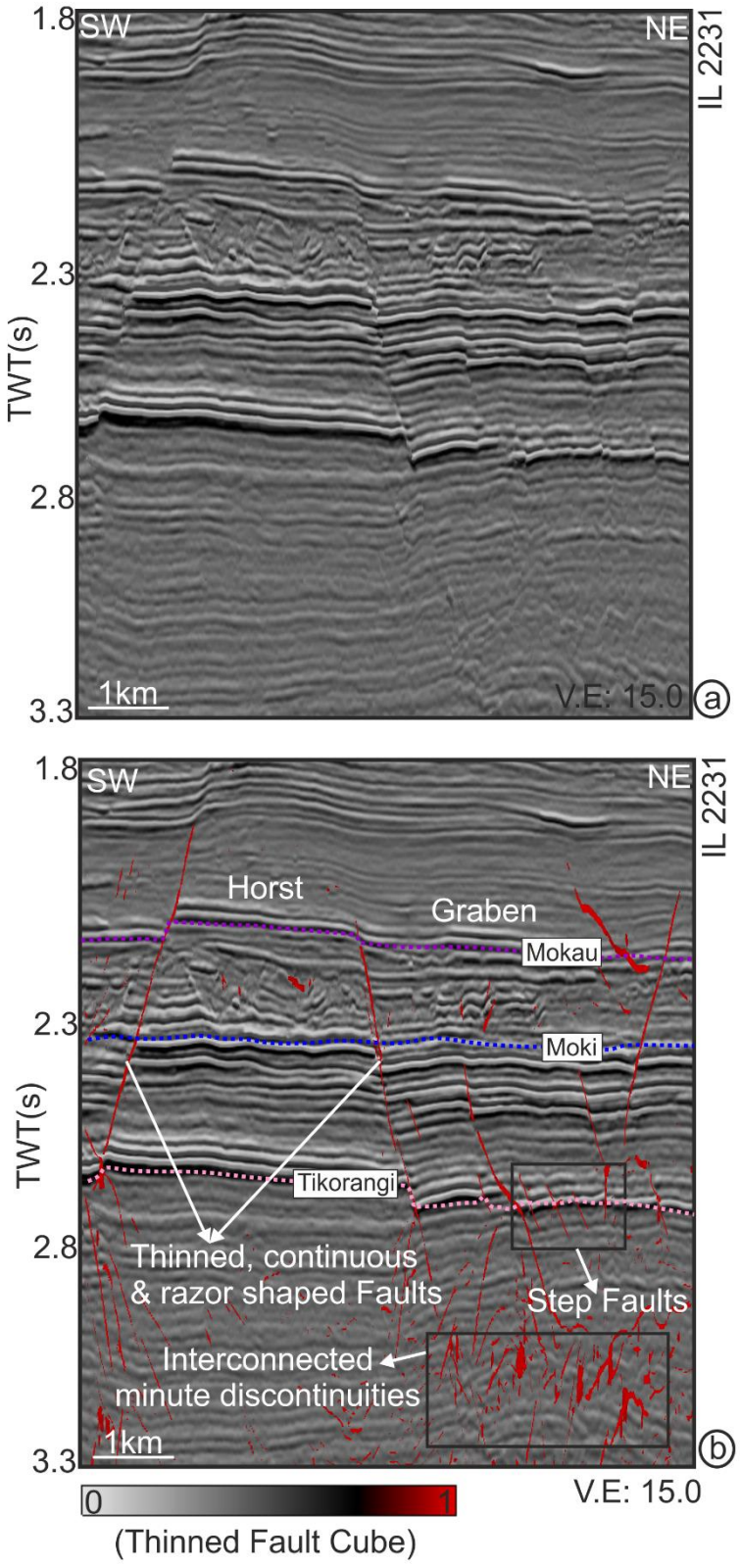

Fig. 11: (a) Uninterpreted seismic line (IL 2231) revealing the subsurface structural compartments; (b) TFC meta-attribute co-rendered with the amplitude data and the relief attribute for the interpreted seismic line (IL 2231). The TFC meta-attribute prominently brings out thin sharpened faults that structurally compartmentalise the Miocene Formations. These faults also intersect the underlying Oligocene Tikorangi Formation.

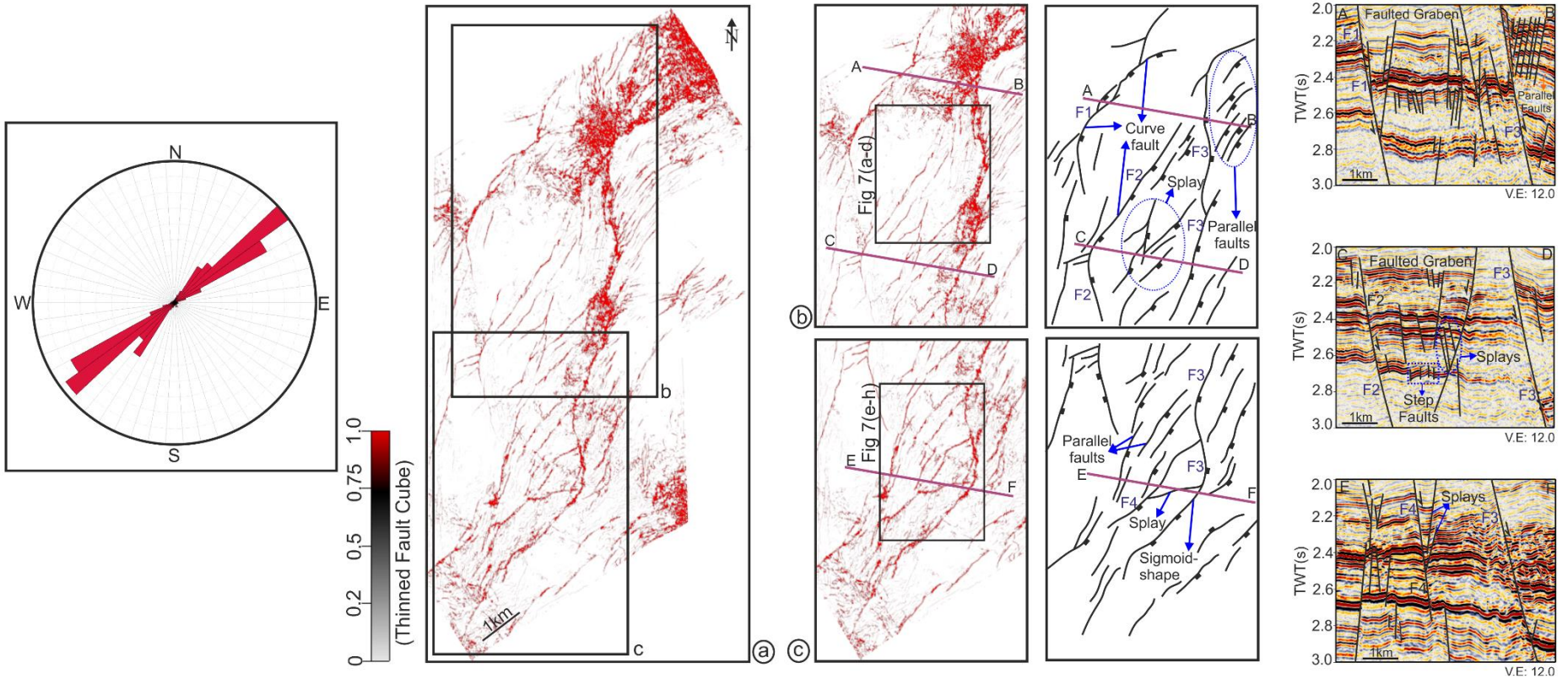

Fig. 12: TFC meta-attribute for the Mokau formation. Faults in the Mokau Formation strike to the NE. (b) Faults in the northern to central parts show a curved pattern (namely F1 and F2). Fault splays are observed in the central part of the formation, and parallel faults are observed towards the NE. Fault F3 is segmented and shows a sigmoidal geometry. (c) Faults towards the southern part are Y-shaped (e.g. F4). F4 is also associated with several splays. The sigmoid-shape of F3 is more prominent in the southern part of the study area.

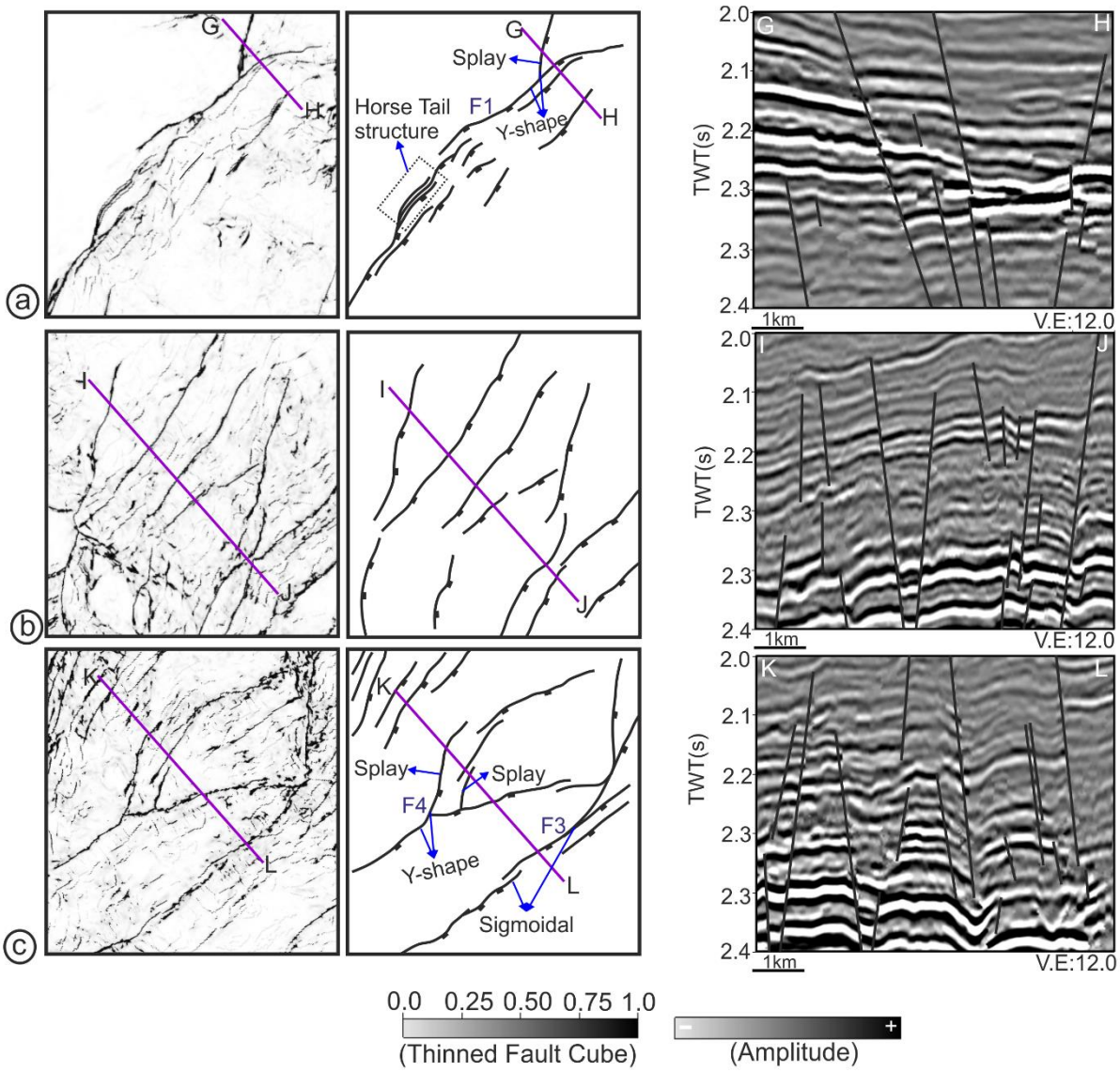

Fig. 13: TFC meta-attribute for a time slice at t=2.1 s. Faults are better appreciated in the three panels (a), (b) and (c). (a) Fault F1 is curved in nature and gave rise to several splays arranged in a Y-shaped pattern. Towards the NW, F1 is linked to several other faults arranged in a horse tail pattern. (b) The central part of the prospect is deformed by several parallel faults. (c) Fault F4 exhibits a Y-shaped geometry with several splays. Fault F3 is segmented and is sigmoidal.

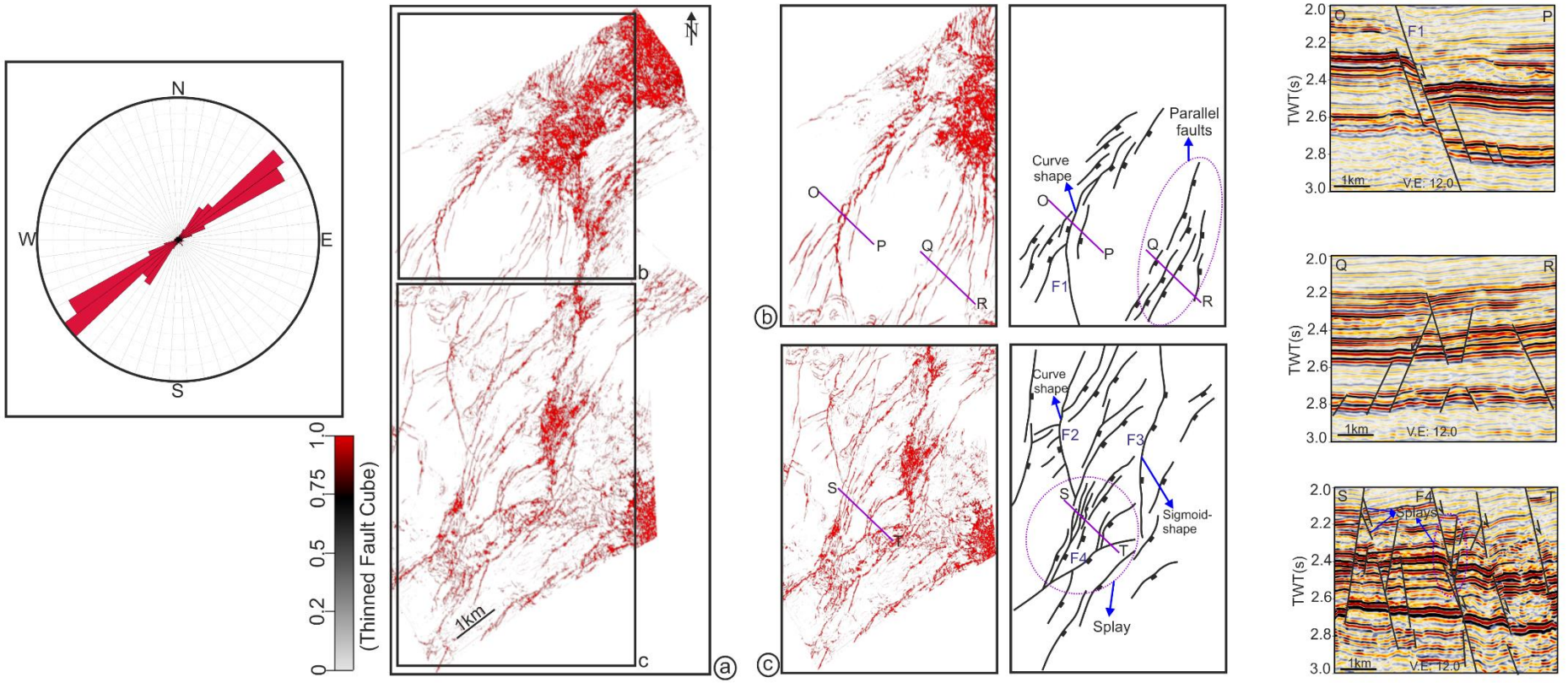

Fig. 14: TFC meta-attribute for the Moki formation. Faults in the Moki Formation strike to the NE. (b) Faults in the northern part of the study area are curved (e.g. F1) and parallel (violet dotted oval); (c) Fault F3 is segmented and sigmoidal. Faults in the south are Y-shaped (e.g. F4). F4 is also associated with several splays (violet dotted oval).

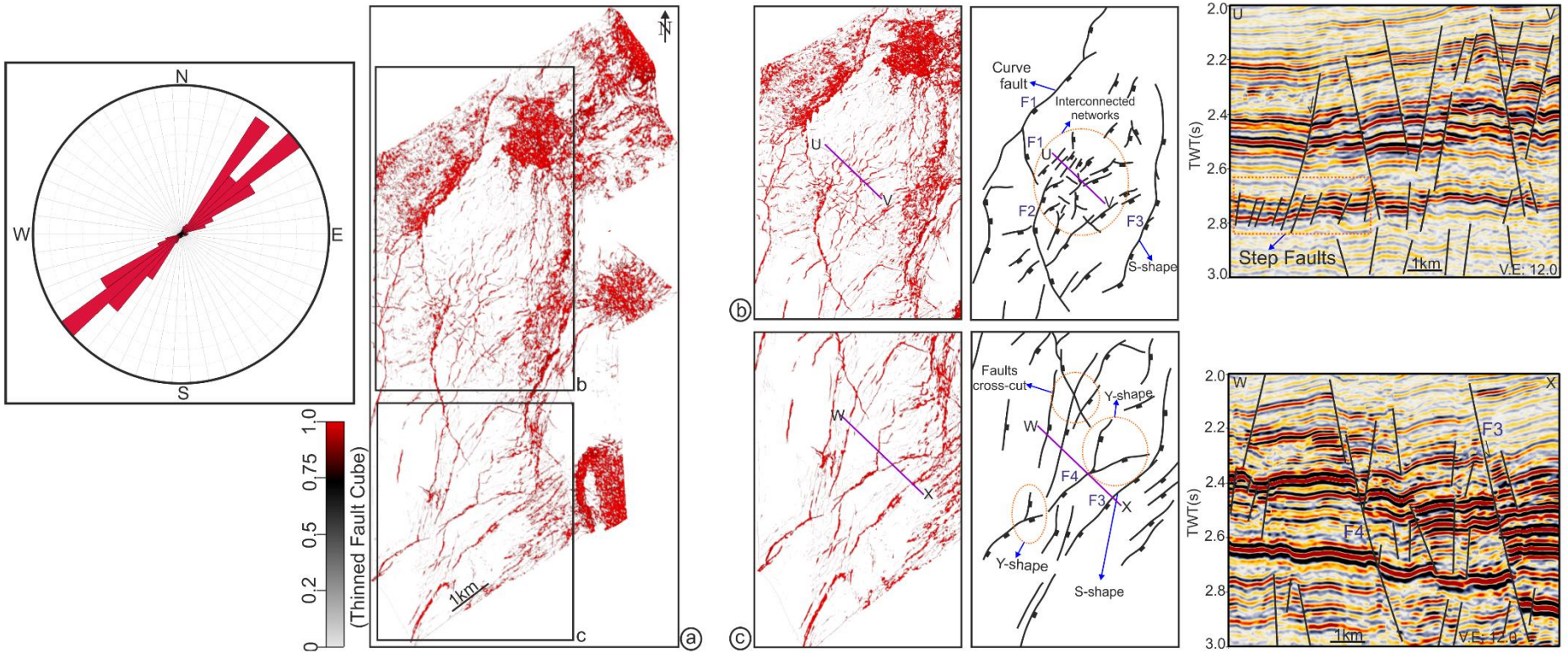

Fig. 15: TFC meta-attribute for the Tikorangi Formation. Faults in the Tikorangi formation strike to the NE; (b) Faults in the north are curved (e.g., F1). The central part of the study area is deformed by a set of closely-spaced en echelon faults. (c) Faults in the south are Y-shaped (orange dotted oval). F4 is Y-shaped and associated with several splays. Fault F3 continues to reveal its sigmoidal shape.

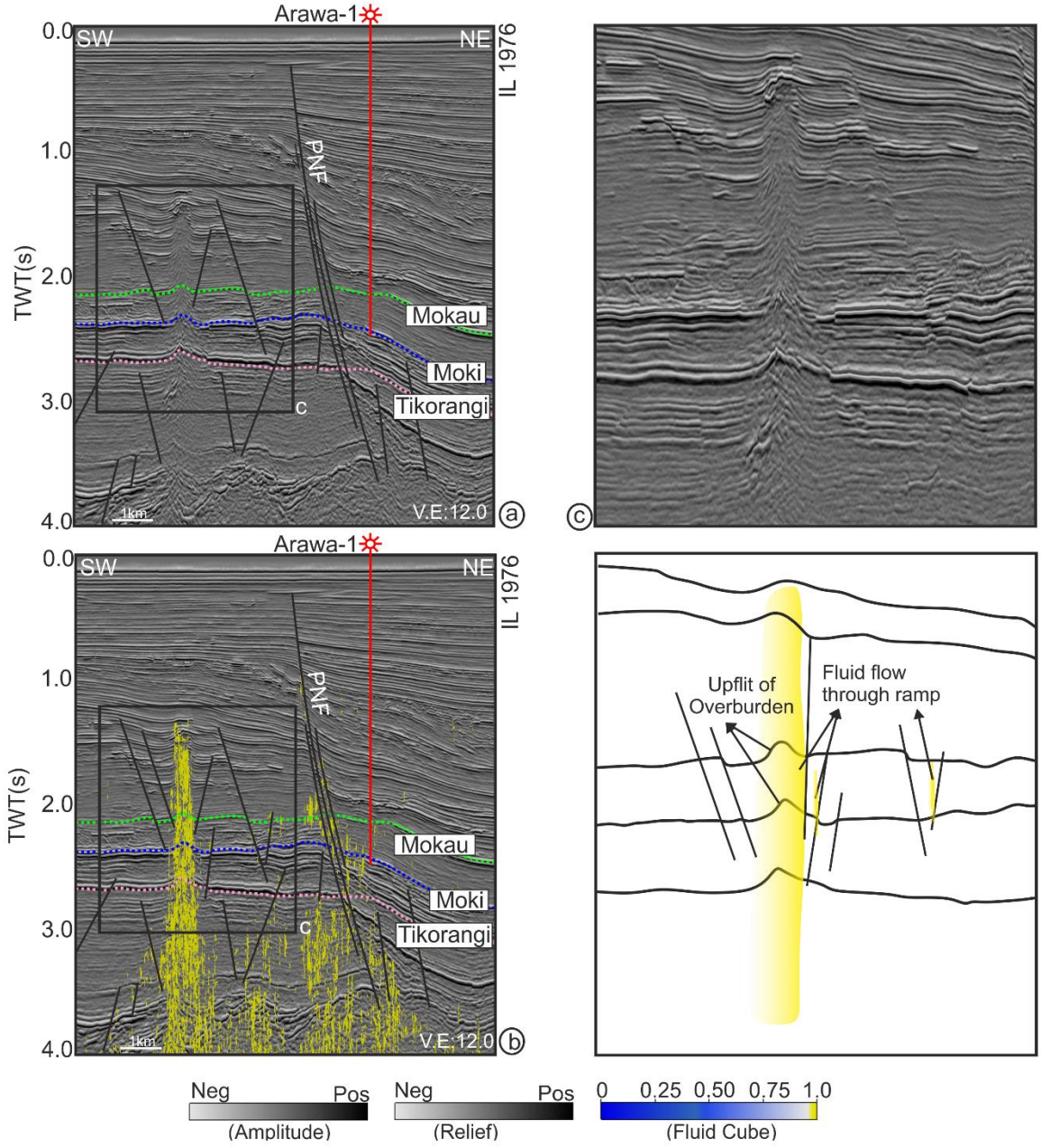

Fig. 16: (a) Interpreted seismic line (IL 1976). Discontinuous fluid zones are observed within the western compartment of the Parihaka prospect. Moreover, the Mokau, Moki and Tikorangi Formations trap the migrating fluid. (b) The FC meta-attribute reveals the true extend of the vertical migration of fluid through the faults. These fluids migrate from older formations (Late Cretaceous-Oligocene) into Miocene strata, and escape into younger successions. Discontinuous breached ramps act as conducive pathways for such fluid migration and leakage; (c) Detailed view of the fluid zone.

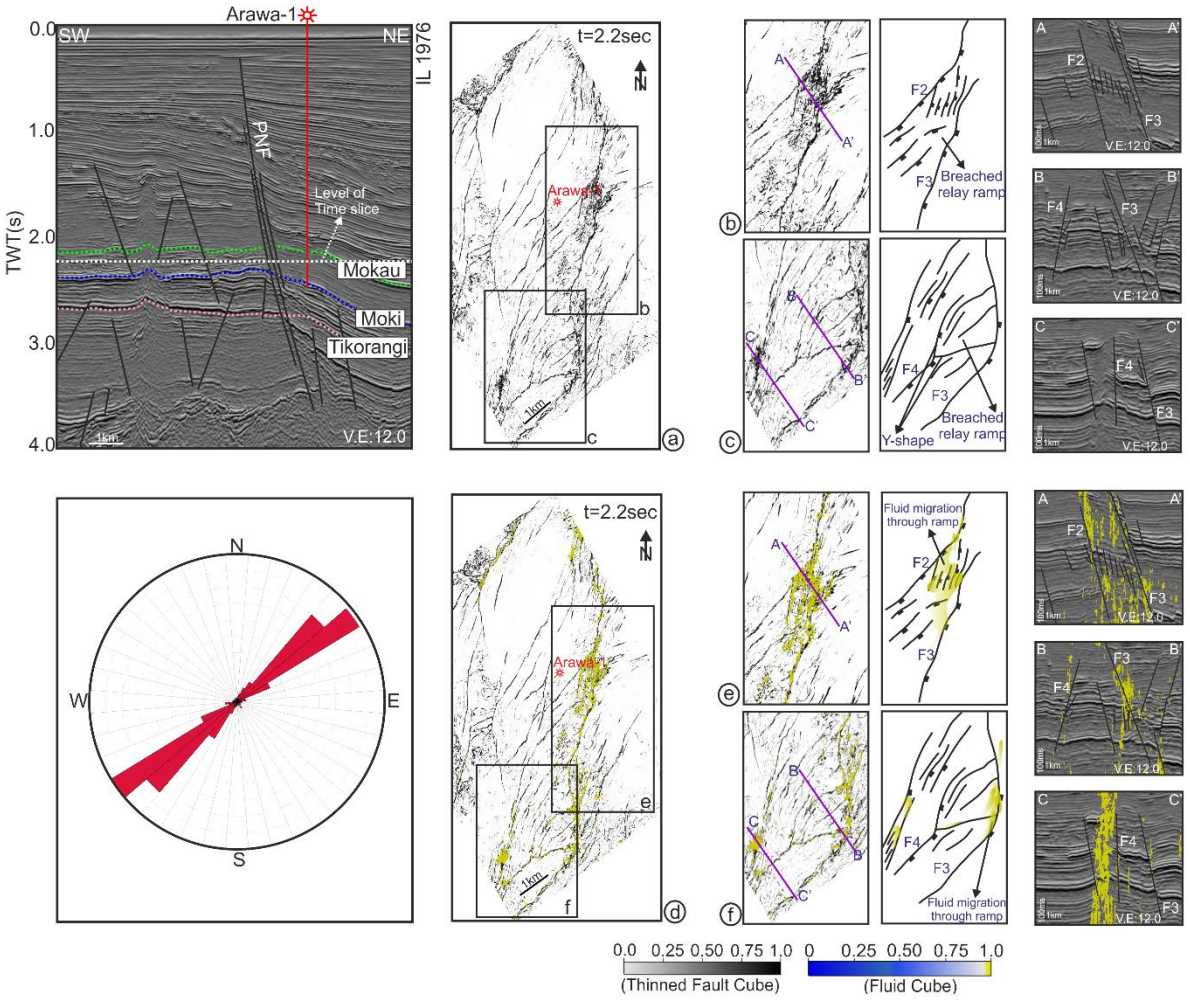

Fig 17: (a) Time slice at t=2.2 s, displayed using the TFC meta-attribute. Faults strike to the NE. (b) The relay ramp between faults F2 and F3 is breached by a set of parallel faults, thereby deforming the ramp towards the NE. (c) The relay ramp between faults F3 and F4 is breached by parallel faults and splays in fault F4, thereby deforming the ramps in the south. (d), (e) & (f) FC meta-attribute co-rendered with the TFC meta-attribute. The breached ramps are associated with high FC probability, suggesting fluid leakage within hard-linked fault zones.

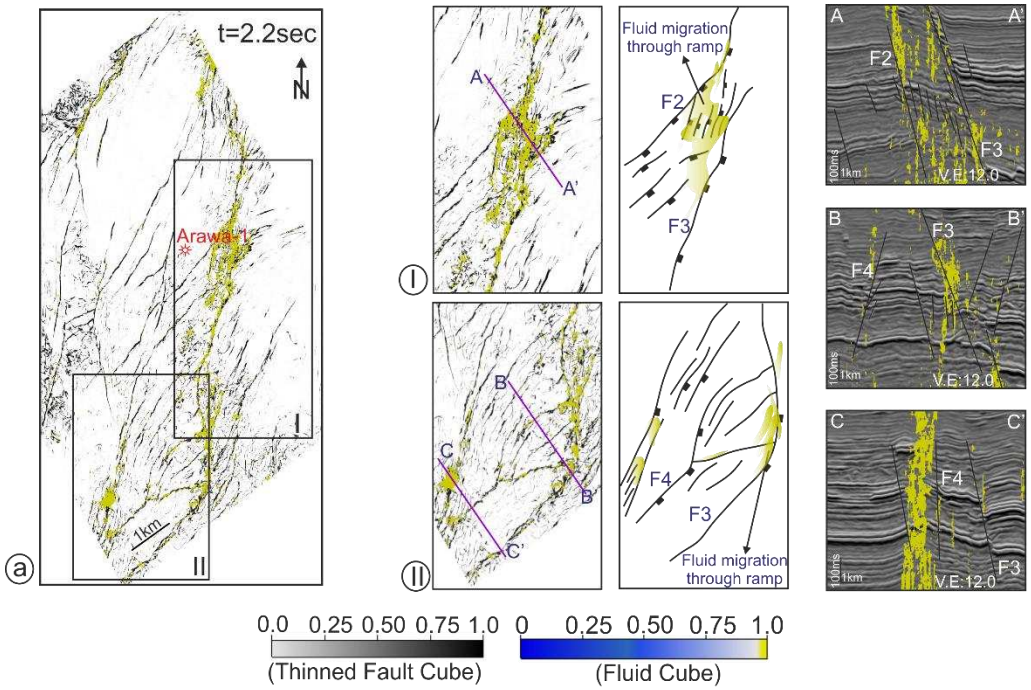

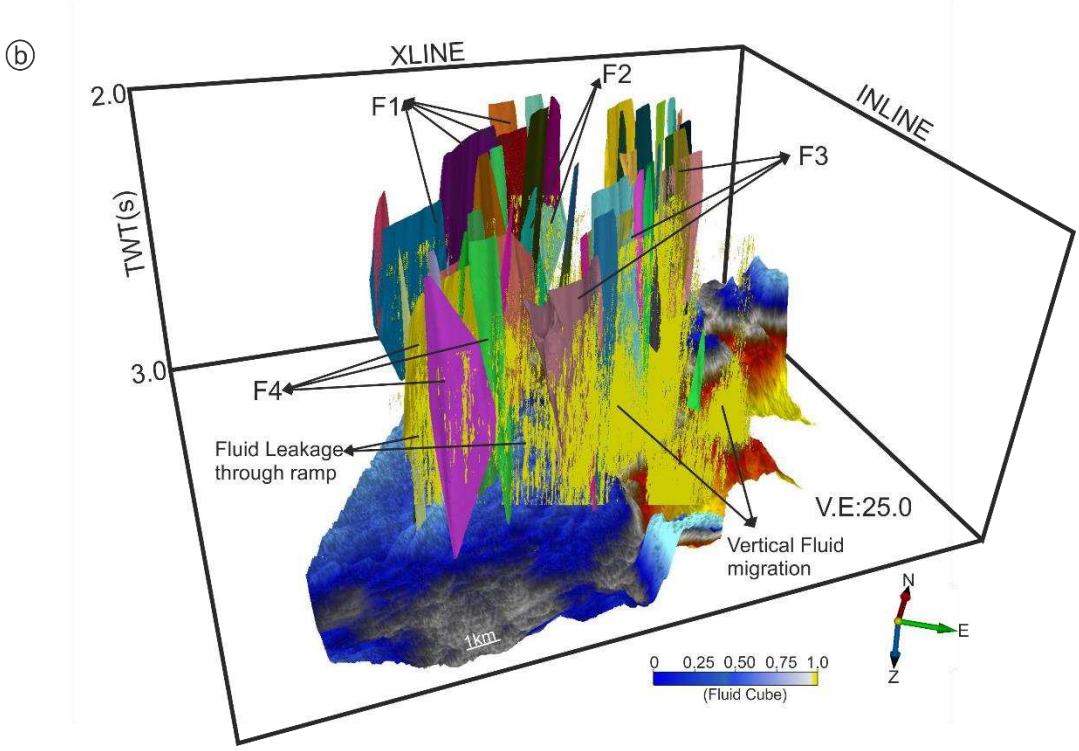

Fig 18: (a) Time slice at t=2.2 s through a co-rendered display of TFC and FC meta-attributes. Fluid flow is revealed through the breached relay ramps. (b) 3D view of fluid leakage through the deformed hard-linked zones of the Miocene interval. Fluid leakage is more pronounced in a NE-SW direction, where faults are segmented and show complex geometries.

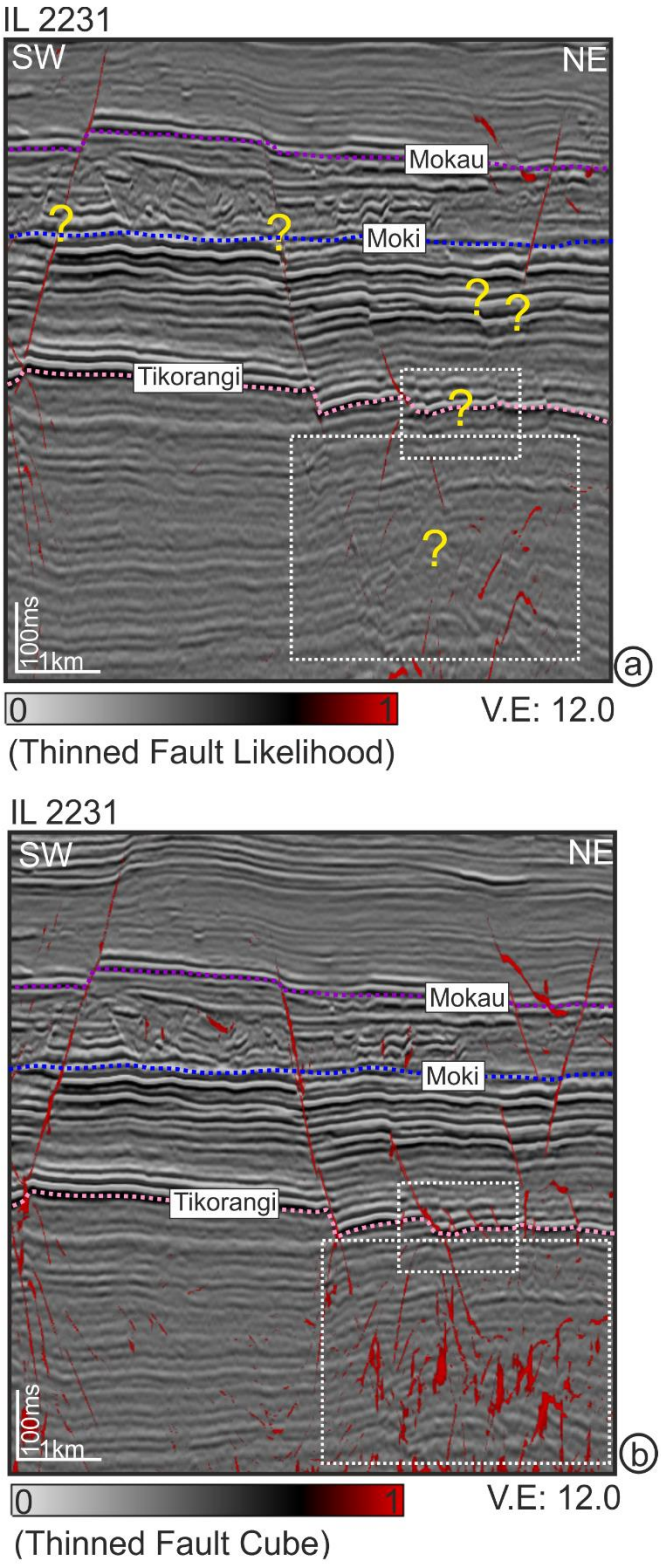

Fig 19: (a) TFL attribute for seismic line IL 2231. Though the TFL bring out thinned fault signatures, in some places (marked with yellow question mark) the structural continuity of faults is poorly captured. Moreover, the attribute fails to bring out the presence of minute structural discontinuities in deeper strata; (b) The TFC attribute fills these gaps by revealing the presence of structural discontinuities, proving to be efficient in comparison to TFL.

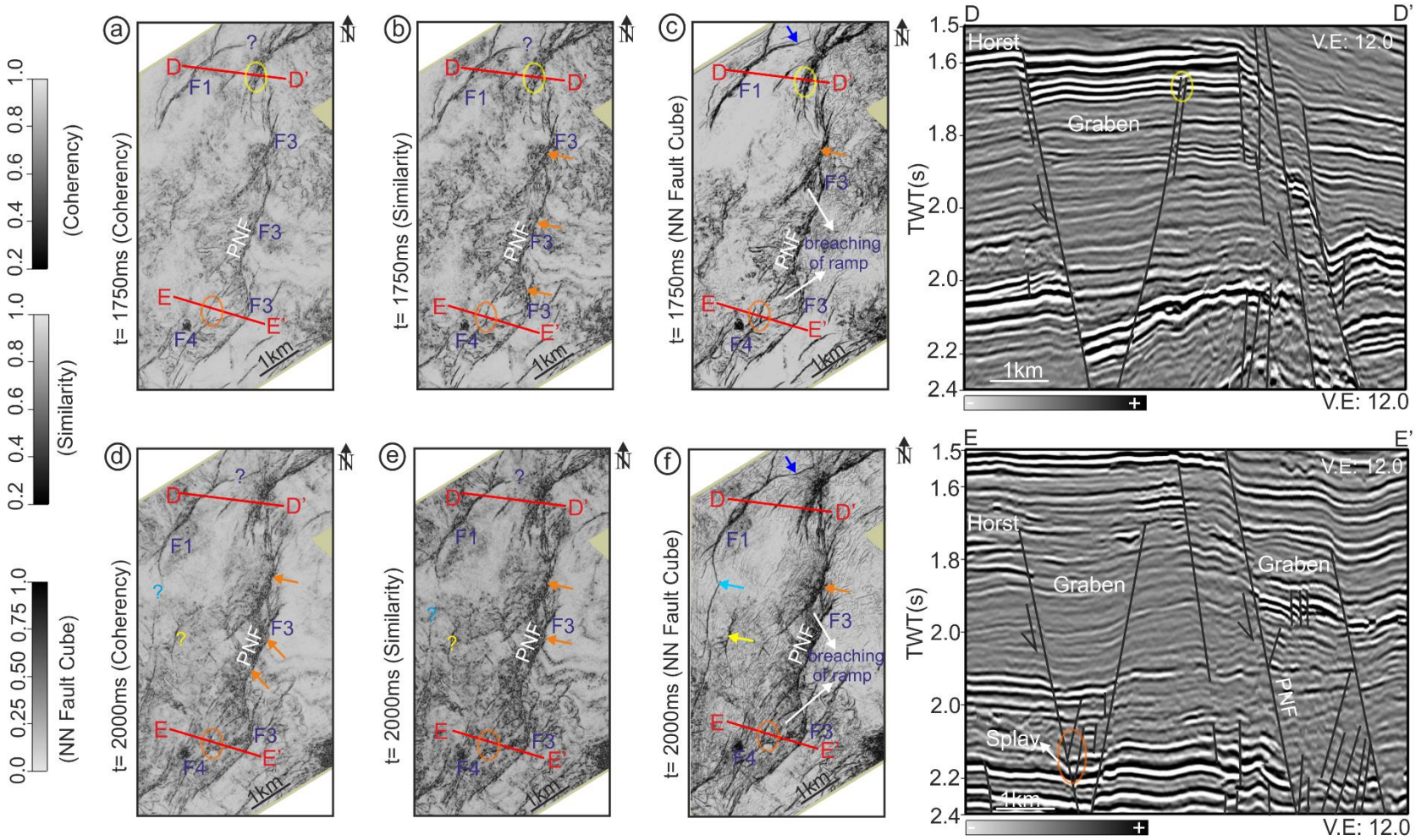

Fig. 20: (a), (b), (c) Time slice at t=1.7 s showing coherency, similarity and TFC attributes. The TFC attribute brings out enhanced images of faulted structures when computed to the individual attributes (a) & (b); (d), (e), (f) A similar enhancement is observed in the time slice at t=2.0 s . Such a comparison highlights the efficacy of meta-attributes over single attribute interpretation. NN-Neural Network.

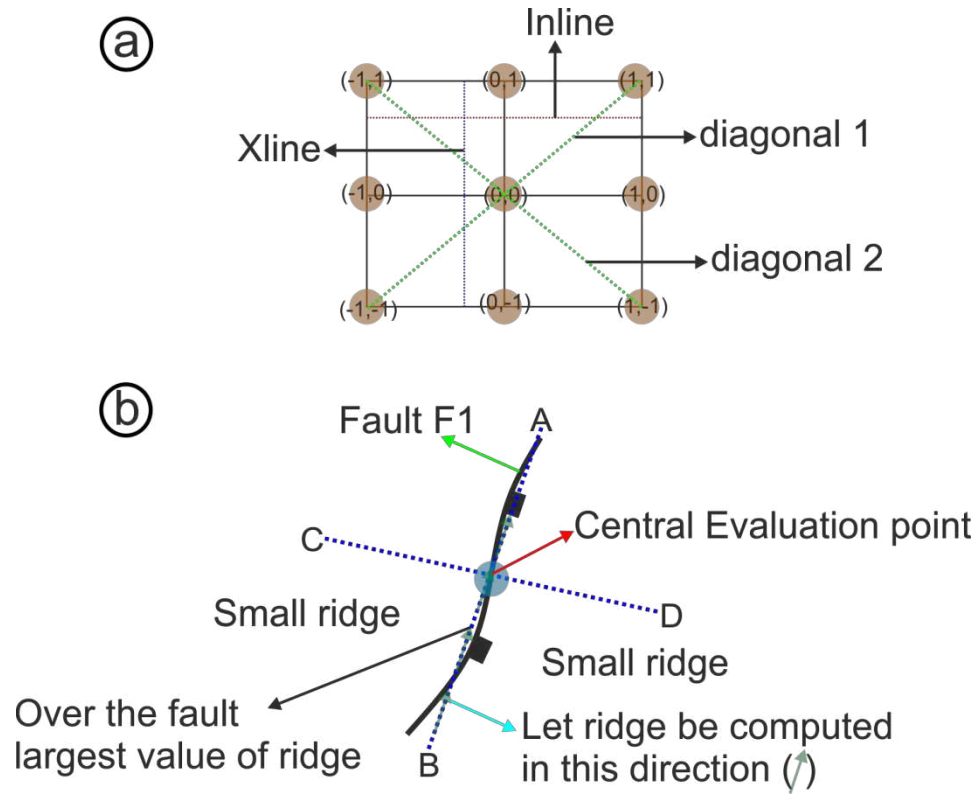

Fig. E.1: (a) Scanning the target by REF in four different directions, i.e. inline, xline and two diagonal lines oriented 45 and 135 degrees in a time-slice domain; (b) Extraction of a ridge (REF) surrounding the central evaluation point.

Table 1: Computation time required to execute the process.

Conditioning of Data (computation time in seconds)		**TFL optimization (computation time in seconds)**		**Multiple attributes (computation time in seconds)**		**Neural Network (run time in seconds)**
Detailed Steering	19916 s	TFL (11,14)	45267 s	REF	13248 s	NN-TFC: 17 s NN- FC: 21 s
Background Steering	36126 s	TFL (21,26)	37524 s	Similarity	18335 s	
DSMF seismic volume	32516 s	TFL (31,34)	92293 s	Energy	2435 s	
DSDF seismic volume	59191 s	TFL (41,50)	92849 s	Avg. Frequency	11496 s	
Similarity attribute	18335 s	TFL (51,60)	261128 s	Reference Time	294 s	
FEF seismic volume	5361 s	----------	----------	Optimized TFL (51,60)	261128 s	

Table 2: Relative contributions offered by each input nodes (seismic attributes) for neural training in the design of the TFC meta-attribute.

Attributes (Input nodes)	**Weights**
TFL	97.2
Similarity LW (Long Window)	93.8
REF	87.2
Signal/Noise	84.5
Similarity MW (Mid Window)	77.3
Reference Time	71.8

Table 3: Relative contributions offered by each input nodes (seismic attributes) for neural training in the design of the FC meta-attribute.

Attributes (Input nodes)	**Weights**
Similarity	96.8
Signal/Noise	92.4
Average Frequency	84.8
Energy	74.2
Reference Time	71.8

Table 4: Identified fault geometry and trends within Miocene strata.

Fault ID	Structural Architecture	Structural Trend	Remarks
F1	Curve shape	N100-120E	The fault contains several splays and breached ramp zones
F2	Curve shape	N110-170E	The fault contains several splays
F3	Sigmoidal/S-shape	N50-70E	The fault is segmented and separates the whole geological sequence into two major eastern and western structural compartments
F4	Y-shaped	N40-60E	The fault is associated with several splays and breached ramps providing pathways for fluid leakage